Inorganic Chemistry

pubs.acs.org/IC

Article

Mitochondria Localized Anticancer Iridium(III) Prodrugs for Targeted Delivery of Myeloid Cell Leukemia-1 (Mcl-1) Inhibitors and Cytotoxic Iridium(III) Complex

Tejal Dixit, Monika Negi, and V. Venkatesh*

Cite This: *Inorg. Chem.* 2024, 63, 24709−24723

Read Online

ACCESS | Metrics & More | Article Recommendations | Supporting Information

ABSTRACT: Myeloid cell leukemia-1 (Mcl-1) is an antiapoptotic oncoprotein overexpressed in several malignancies and acts as one of the promising therapeutic targets for cancer. Even though there are several small molecule based Mcl-1 inhibitors reported, the delivery of Mcl-1 inhibitor at the target site is quite challenging. In this regard, we developed a series of mitochondria targeting luminescent cyclometalated iridium(III) prodrugs bearing Mcl-1 inhibitors via ester linkage due to the presence of Mcl-1 protein in the outer mitochondrial membrane. Among the synthesized prodrugs, IrThpy@L2 was found to exhibit the potent cytotoxicity (IC_{50} = 30.93 nM) against HCT116 cell line when compared with bare Mcl-1 inhibitors (IC_{50} > 100 μM). Mechanistic studies further revealed that IrThpy@L2 quickly gets internalized inside the mitochondria of HCT116 cells and undergoes activation in the presence of overexpressed esterase which leads to the release of two cytotoxic species i.e. Mcl-1 inhibitors (I-2) and cytotoxic iridium(III) complex (IrThpy@OH). The improved cytotoxicity of IrThpy@L2 is due to the mitochondria targeting ability of iridium(III) prodrug, subsequent esterase activated release of I-2 to inhibit Mcl-1 protein and IrThpy@OH to generate reactive oxygen species (ROS). After prodrug activation, the released cytotoxic species cause mitochondrial membrane depolarization, activate a cascade of mitochondria-mediated cell death events, and arrest the cell cycle in S-phase which leads to apoptosis. The potent anticancer activity of IrThpy@L2 was further evident from the drastic morphological changes, size reduction in the solid tumor mimicking 3D multicellular tumor spheroids (MCTS) of HCT116.

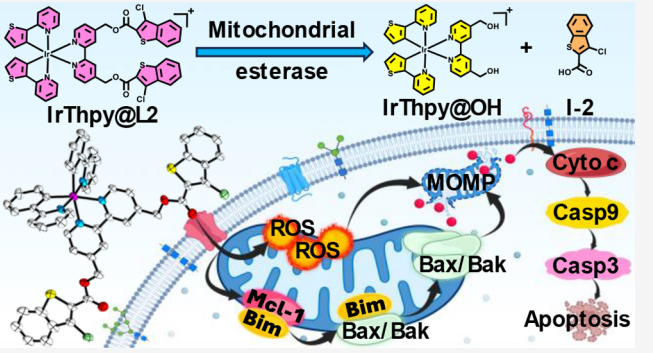

INTRODUCTION

Protein−protein interactions (PPIs) play a pivotal role in several cellular processes like signal transduction, enzymatic activity, structural organization, gene regulation, protein folding, and quality control, etc., enabling cells to carry out their functions and respond to environmental cues.[1−4] These interactions occur when two or more proteins bind together via specific binding sites, which help to regulate cellular processes such as cell growth, differentiation, and apoptosis. Dysregulation or disruption of normal protein−protein interactions can lead to various molecular and cellular changes like activation of oncogenic signaling pathways, dysregulation of apoptosis and cell cycle control, disruption of tumor suppressor functions, activation of angiogenesis and metastasis that promote tumor growth and progression.[5] Understanding the aberrant protein−protein interactions involved in tumorigenesis is crucial for developing targeted therapies that can selectively disrupt or modulate these interactions to inhibit tumor growth.

Researchers are actively studying these interactions to identify potential therapeutic targets and develop strategies to interfere with their associations. One such strategy is the development of small molecule inhibitors to target these PPIs.[5] However, it is difficult to target these PPIs as their binding sites are usually wide and shallow,[6] making it difficult for the small molecules to interact.[7,8] Therefore, it is a great challenge to design small molecules that can inhibit these PPIs with high selectivity and good binding affinity.

Antiapoptotic proteins play significant role for the survival and progression of tumor by engaging cross talk with pro-apoptotic proteins, which makes them appealing targets in several cancer therapies.[9−11] Mcl-1 is one such critical antiapoptotic protein that belongs to the Bcl-2 family of proteins that is generally overexpressed in various cancers like estrogen receptor-positive breast cancer, melanoma, leukemia, nonsmall cell lung cancer, ovarian, liver, colorectal, and human cervical cancers, etc.[12−14] In cancer cells, the overexpression of

Received: September 18, 2024
Revised: November 6, 2024
Accepted: December 2, 2024
Published: December 12, 2024

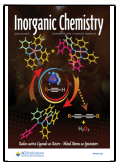

https://doi.org/10.1021/acs.inorgchem.4c03950
Inorg. Chem. 2024, 63, 24709−24723

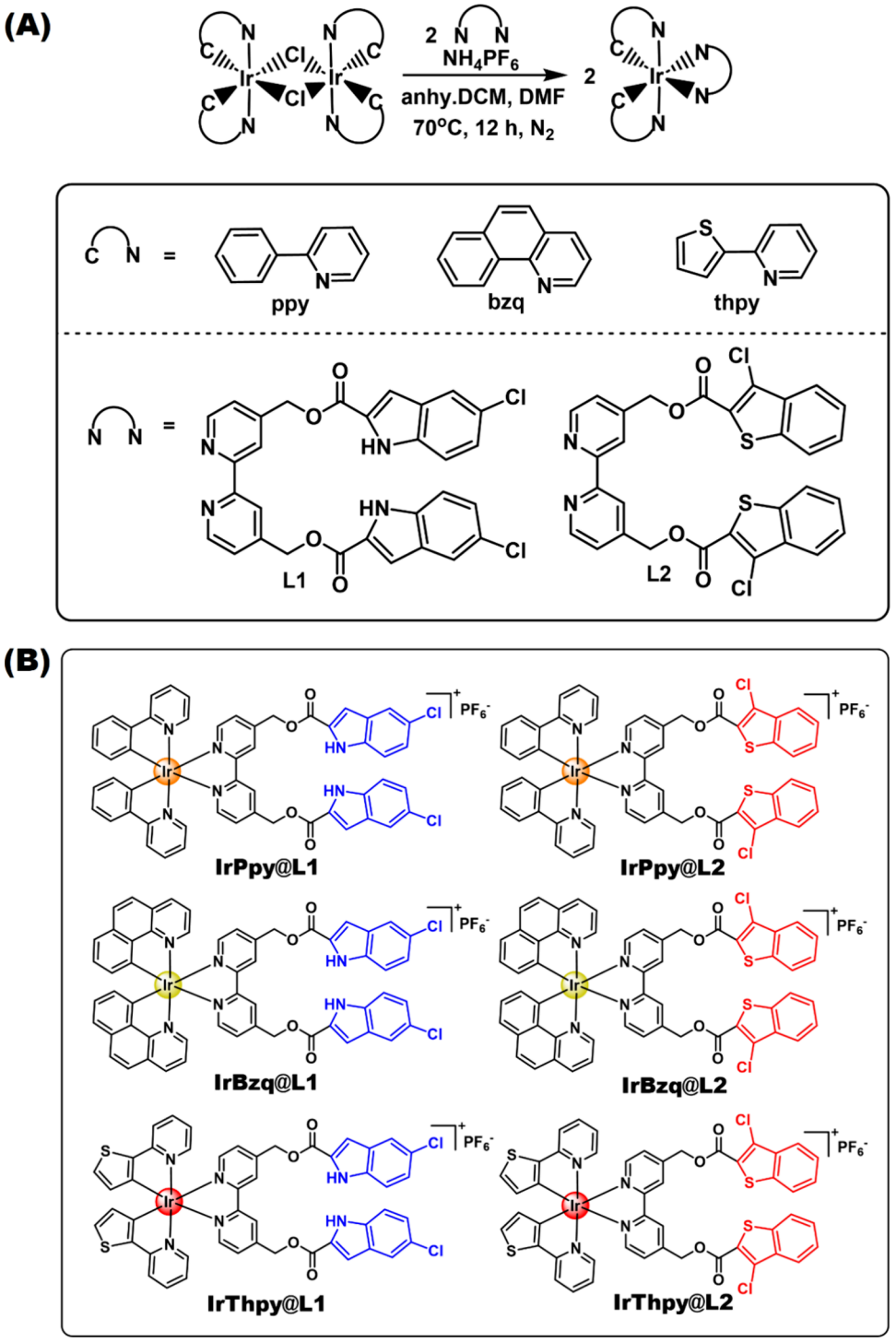

Figure 1. (A) Synthetic scheme for the preparation of Ir(III) prodrugs. (B) Molecular structure of all six synthesized iridium(III) prodrugs.

Mcl-1 can contribute to tumor growth, resistance to radiotherapy, chemotherapy, and reduced patient survival rates.[15,16] Its upregulation allows cancer cells to evade programmed cell death, thereby promoting their survival and contributing to tumor progression.[17,18] Due to its crucial role in cancer cell survival, targeting Mcl-1 protein has become an intense area of research in anticancer therapies.[19,20] Researchers are actively developing Mcl-1 inhibitors which could bind Mcl-1 protein effectively and with high degree of selectivity.[21] In this direction, several small molecule inhibitors have been developed to target the Mcl-1 protein and inhibit the PPIs through which it exerts its activity, but until now, no Mcl-1 inhibitor has been approved for clinical applications.[22,23] Some of them have entered clinical trials (AZD5991, AMG-176, NCT03218683, and NCT03797261), but unfortunately got terminated due to their severe side effects.[24] There are several drawbacks associated with small molecule based Mcl-1 inhibitors such as low bioavailability, low membrane permeability, and off-target bindings, etc.[25] Recent studies have shown that most of the Mcl-1 inhibitors lack proper mitochondrial membrane penetration, and exhibit poor anticancer activity.[26] Therefore, not only structural modifica-

https://doi.org/10.1021/acs.inorgchem.4c03950
Inorg. Chem. 2024, 63, 24709−24723

tion to enhance the binding affinity with Mcl-1 protein but also more attention is required for the proper organelle targeting ability of Mcl-1 inhibitors. Over the past decade, there has been a great leap in the discovery of small molecule-based inhibitors. Several small molecules such as benzothiophene-2-carboxylic acid, indole-2-carboxylic acid, benzofuran-2-carboxylic acid, and their derivatives were identified as potent Mcl-1 inhibitors.[27] But, delivering them in the mitochondria is of paramount importance for eliciting potent anticancer activity.[28]

After the success of Cisplatin in the anticancer arena, various other metal-based anticancer complexes have captivated the attention of researchers over the past few decades.[29−41] The anticancer activity of iridium(III) complexes have been extensively studied because of their diverse mechanism of action, kinetic stability in biological systems which can be considered further as potential alternative for conventional platinum-based anticancer drugs to overcome the side effects and drawbacks of platinum resistance.[42−47] Cyclometalated iridium(III) complexes have demonstrated significant anticancer activity against a variety of cancer types, including both solid tumors and leukemic cells, as they penetrate the cancer cells and target various subcellular organelles.[48−53] They can induce cancer cell death through multiple modes of action, different from those of conventional platinum drugs, including apoptosis (programmed cell death), autophagy (self-degradation of cellular components), inhibition of protein−protein interactions, and disruption of cellular signaling pathways.[54−66] Furthermore, these complexes have opulent photophysical properties,[67] including high quantum yields,[68,69] good photostability,[70,71] long emission lifetimes,[72,73] large Stokes shifts,[74] two-photon absorption (TPA), and high photobleaching resistance[75] making them effective candidates for cancer imaging and diagnostics.[76−80]

Considering all of the above aspects, we have designed and synthesized mitochondria targeting cyclometalated iridium(III) complexes bearing Mcl-1 inhibitors as prodrugs. The positive charge on the cyclometalated iridium(III) prodrugs favors its mitochondria-targeting ability which is also strategically a prominent target in several cancer therapies. This approach facilitates the better uptake of prodrugs[81] due to improved lipophilicity, imparts mitochondria localizing ability,[82] and mitochondrial esterase mediated delivery of Mcl-1 inhibitors at the target site.[83−85]

In this work, six positively charged cyclometalated iridium(III) prodrugs IrPpy@L1, IrPpy@L2, IrBzq@L1, IrBzq@L2, IrThpy@L1, IrThpy@L2 (L1 and L2 = 2,2′-bipyridine-4,4′-diester derivatives of 5-chloroindole-2-carboxylic acid (I-1), and 3-chlorobenzo[b]thiophene-2-carboxylic acid (I-2) respectively) were synthesized (Figure 1B). Complexes IrPpy@OH, IrBzq@OH, and IrThpy@OH which lack the inhibitor part and are already known for their cytotoxicity were also synthesized as reference compounds.[86] IrThpy@L2 was found to be the most potent complex and showed excellent cytotoxicity against the HCT116 cell line. Fluorescence studies and HRMS studies were conducted to investigate esterase mediated activation of prodrug IrThpy@L2 *in vitro*. The photophysical properties, cellular uptake studies, subcellular localization, *in vitro* cytotoxicity, mitochondrial outer membrane permeabilization (MOMP), ROS generation, cell cycle arrest, and bioimaging studies were carried out to understand the mode of action of IrThpy@L2.

RESULTS AND DISCUSSION

Design, Synthesis and Characterization. Herein, Mcl-1 inhibitor appended cyclometalated Ir(III) prodrugs were prepared in two steps. First, The μ-chlorido-bridged dimers $[(ppy)_2\text{-Ir-}\mu\text{-Cl}]_2$, $[(bzq)_2\text{-Ir-}\mu\text{-Cl}]_2$ and $[(thpy)_2\text{-Ir-}\mu\text{-Cl}]_2$ were synthesized from $IrCl_3.xH_2O$ using the procedure reported by us previously.[87] The esterification of Mcl-1 inhibitors (5-chloroindole-2-carboxylic acid (I-1) and 3-chlorobenzo[b]thiophene-2-carboxylic acid (I-2) with 4,4′-Bis(hydroxymethyl)2,2′-bipyridine was carried out to prepare L1 and L2 respectively (N^N ligands).[88] Ir(III) prodrugs were synthesized using $[(ppy)_2\text{-Ir-}\mu\text{-Cl}]_2$, $[(bzq)_2\text{-Ir-}\mu\text{-Cl}]_2$ and $[(thpy)_2\text{-Ir-}\mu\text{-Cl}]_2$ along with L1 and L2 as mentioned in (Figure 1A, S1). All the synthesized complexes were further characterized by ^{1}H & ^{13}C NMR, High-resolution mass spectrometry (HRMS) (Figure S2−S34), and the structure of IrPpy@L2 was confirmed from single crystal XRD.

Single-Crystal X-Ray Diffraction Studies. The single crystal of IrPpy@L2 was grown by using a slow evaporation method in a DCM-toluene (1:1, v/v) solvent mixture. The crystal structure of IrPpy@L2 is shown (Figure 2A). IrPpy@L2

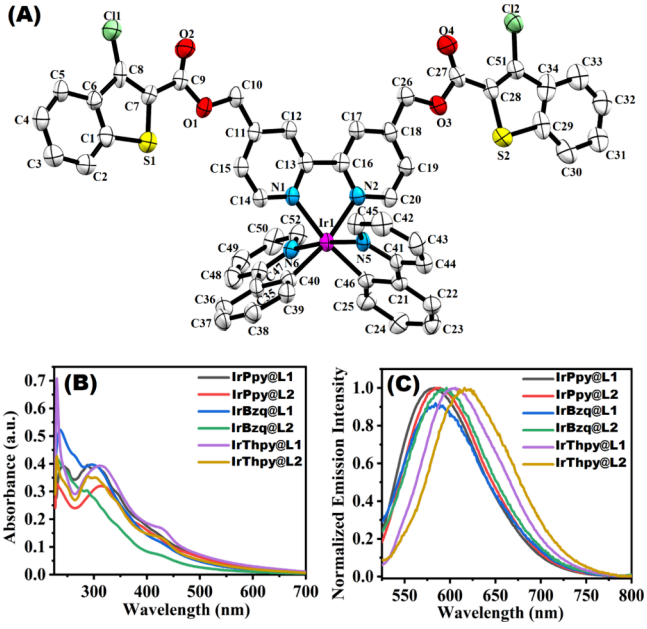

Figure 2. (A) X-ray crystal structure of IrPpy@L2 at a 50% thermal ellipsoids probability level (hydrogen atoms were omitted for clarity). (B, C) Absorption and emission spectra of designed iridium(III) prodrugs (10 μM) performed in DMSO/PBS (v/v, 0.4:99.6) at room temperature.

crystallized in the monoclinic P 1 21/c 1 space group. The details of single crystal data refinement parameters are summarized in (Table S1). The selected bond lengths and bond angles for IrPpy@L2 are provided in (Table S2).

Photophysical Properties. The absorption and emission properties of iridium(III) prodrugs were studied in DMSO/PBS (v/v, 0.4:99.6) (Figure 2B, C) and DMSO (Figure S35A, B) at room temperature. In all the iridium(III) prodrugs, the higher energy intense absorption bands that lie in the UV−vis region of <350 nm could be attributed to the mixed spin-allowed ligand-centered (LC) transition ($\pi-\pi^*$) for C^N and N^N ligands.[89,90] The less intense absorption bands falling between low energy region of UV−vis i.e. 350−450 nm

https://doi.org/10.1021/acs.inorgchem.4c03950
Inorg. Chem. 2024, 63, 24709−24723

(DMSO) and 400−600 nm (DMSO/PBS, 0.4%) is due to mixed singlet and triplet metal-to-ligand charge transfer (^{1}MLCT and ^{3}MLCT) transitions.[91] All six synthesized complexes display bright fluorescence emission maximum between 580 and 620 nm after exciting at 405 nm. Notably, IrThpy@L2 has a bathochromic shifted (red-shifted) emission maxima at 620 nm as compared to the rest of the prodrugs, suggesting that the combination of thpy ligand with L2 causes this shift. All of the prodrugs possess a large Stokes shift of about 200 nm. Emission quantum yields of all the iridium(III) prodrugs range from 0.007 to 0.065 in aerated DMSO at room temperature (Table S3). Moreover, the emission quantum yield of all the synthesized Ir(III) complexes were compared with the respective reference complexes in DMSO/PBS (0.4%) at room temperature (Table S3). Notably, they were found to be 2.4 to 4.5 times higher than their corresponding reference complexes; the observed difference may be due to the presence of substituted N^N ligands. Overall, the synthesized prodrugs hold good photophysical properties which could be utilized to understand their subcellular localization.

Lipophilicity and Cellular Uptake. Inductively coupled plasma mass spectrometry (ICP-MS) was utilized to quantitatively estimate the cellular uptake of the iridium(III) prodrugs. HCT116 cells were incubated with 5 μM iridium-(III) prodrugs for 1 h. It was observed that the accumulation of iridium inside cells in nM/7 × 10^4cells is highest for IrThpy@L2 compared to others (Figure 3A) and (Table S3). This higher accumulation of IrThpy@L2 could be attributed to its higher lipophilicity compared to others as the water-octanol partition coefficient value (log $P_{o/w}$) follows the order IrThpy@L2 > IrThpy@L1 > IrPpy@L2 > IrBzq@L2 > IrPpy@L1 > IrBzq@L1 (Table S3). The uptake of iridium(III) prodrugs in HCT116 cells correlates well with their lipophilicity.

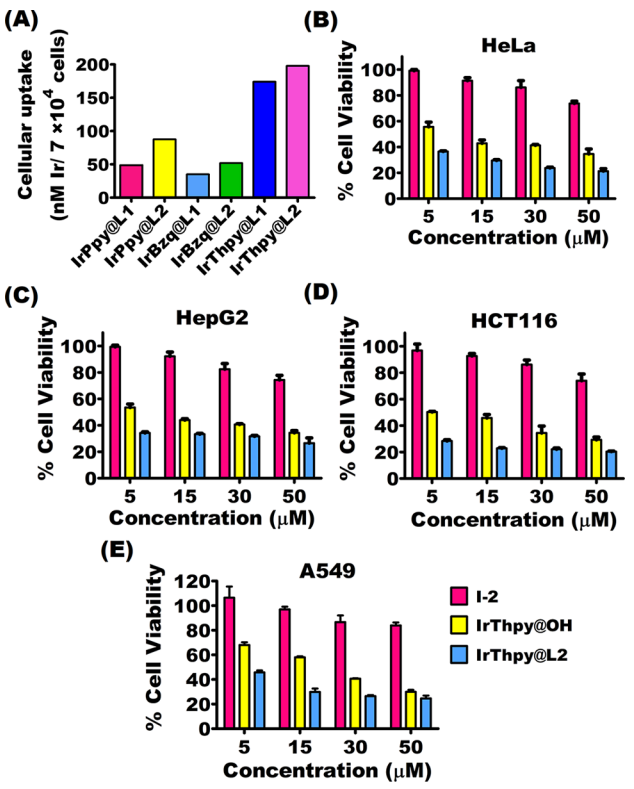

Figure 3. (A) The cellular uptake of iridium(III) prodrugs in HCT116 cells after exposure to IrPpy@L1, IrPpy@L2, IrBzq@L1, IrBzq@L2, IrThpy@L1, and IrThpy@L2 for 1 h (5 μM each). (ICP-MS was used to determine the concentration of iridium). (B, C, D, E) Cell viability assay was performed for IrThpy@L2, IrThpy@OH, and I-2 against HeLa, HepG2, HCT116, and A549 cells after 48 h treatment.

***In-Vitro* Cytotoxicity.** The cytotoxicity of all six synthesized iridium(III) prodrugs, their corresponding reference complexes, inhibitors, and Cisplatin was studied against HeLa (Human Cervical Carcinoma), HepG2 (Human Hepatocellular Carcinoma), HCT116 (Human Colorectal Carcinoma), A549 (Human Pulmonary Carcinoma), and human normal liver cells (WRL-68) with the help of the MTT (3-(4,5-dimethylthiazole-2-yl)-2,5-diphenyltetrazolium bromide) assay. The half-maximum inhibitory concentration (IC_{50}) values after 48 h of iridium(III) prodrugs treatment are listed in (Table 1) and (Figure 3B,C,D,E). All the iridium(III) prodrugs showed good antiproliferative activity against all the tested cancer cell lines, especially against HCT116 cell line with the IC_{50} values lying between 0.03 to 7.06 μM. Among all six iridium(III) prodrugs, IrThpy@L2 has shown the best activity against HCT116 cancer cell line. The IC_{50} value of IrThpy@L2 against the HCT116 cell line is 600-fold and 200-fold less than that of Cisplatin and its corresponding reference complex (IrThpy@OH) respectively. These results suggest that IrThpy@L2 has the substantial capability to induce cytotoxicity against HCT116 cell line whereas both the Mcl-1 inhibitors, I-1 and I-2 were found to be nontoxic even at higher concentrations. This could be attributed to their lower lipophilicity and off-target bindings. As the HCT116 cell line contains ample amount of esterase and overexpressed Mcl-1 protein,[92−95] therefore, the hydrolysis of IrThpy@L2 is feasible and further releases cytotoxic species which lead to the generation of ROS and Mcl-1 inhibition that resulted in nanomolar toxicity. All of the complexes were found to be more selective for the human cancer cell line as compared to the human normal cell (WRL-68) (Table 1) and (Table S4). The selectivity of the complexes is mainly due to the prodrug strategy developed in this approach, which results in higher IC_{50} values for normal cells. Due to aberrant metabolic activities and altered mitochondrial functions, cancer cells produce elevated levels of esterase and Mcl-1 protein when compared with normal cells.[76,83,96−102] Therefore, cancer cells provide an ideal environment to activate prodrug and exhibit nanomolar toxicity. These results thus confirmed our strategy of appending Mcl-1 inhibitors to the iridium scaffold for simultaneously inhibiting Mcl-1 protein and elevating ROS for inducing mitochondria mediated cell death selectively in cancer cells.

Most notably, the cytotoxicity of iridium(III) prodrugs correlates well with their cellular uptake and lipophilicity. IrThpy@L2 exhibited potent cytotoxicity with highest uptake against HCT116 cell line; therefore, it has been considered as a lead molecule to perform further biological studies.

***In-Vitro* Activation of IrThpy@L2 Prodrug.** In all of the designed iridium(III) prodrugs, Mcl-1 inhibitors are attached via ester linkage. Therefore, they undergo hydrolysis in the presence of mitochondrial esterase after reaching the mitochondria. Herein, porcine liver esterase (PLE) was used to study the hydrolysis of ester bonds in IrThpy@L2 as depicted in (Figure 4D). To validate the esterase mediated release of Mcl-1 inhibitors *in vitro*, HRMS and fluorescence

https://doi.org/10.1021/acs.inorgchem.4c03950
Inorg. Chem. 2024, 63, 24709−24723

Table 1. IC_{50} (μM) of the Synthesized Complexes, Inhibitors, and Cisplatin Against HCT116, HepG2, HeLa, A549, and WRL-68 Cell Lines Expressed as Mean ± Standard Deviation (n = 3) at 48 h

Compounds	IC_{50} (μM)				
	HCT116	HepG2	HeLa	A549	WRL-68
IrPpy@L1	4.22 ± 0.91	6.05 ± 1.10	7.28 ± 1.00	10.83 ± 1.57	>50
IrPpy@L2	0.41 ± 0.23	1.29 ± 0.14	2.05 ± 0.84	8.99 ± 3.33	49.38 ± 2.82
IrBzq@L1	7.06 ± 3.31	9.84 ± 1.83	10.51 ± 1.49	15.65 ± 1.38	>50
IrBzq@L2	2.25 ± 1.92	3.43 ± 1.18	4.86 ± 2.42	9.00 ± 1.07	>50
IrThpy@L1	1.94 ± 0.72	2.15 ± 1.52	4.08 ± 2.33	6.18 ± 1.69	44.17 ± 1.97
IrThpy@L2	0.03 ± 0.01	0.05 ± 0.01	0.97 ± 0.75	2.93 ± 1.55	39.18 ± 0.62
IrPpy@OH	7.94 ± 1.76	9.31 ± 1.96	11.39 ± 1.08	22.91 ± 0.97	30.54 ± 0.33
IrBzq@OH	11.52 ± 1.36	16.17 ± 1.06	17.68 ± 0.57	23.62 ± 1.64	35.5 ± 1.35
IrThpy@OH	6.27 ± 2.07	7.66 ± 1.18	8.67 ± 2.16	17.82 ± 1.01	23.22 ± 0.48
Cisplatin	18.01 ± 2.18	18.28 ± 2.33	16.87 ± 0.43	25.87 ± 0.88	22.33 ± 0.35
I-1	>100	>100	>100	>100	>100
I-2	>100	>100	>100	>100	>100

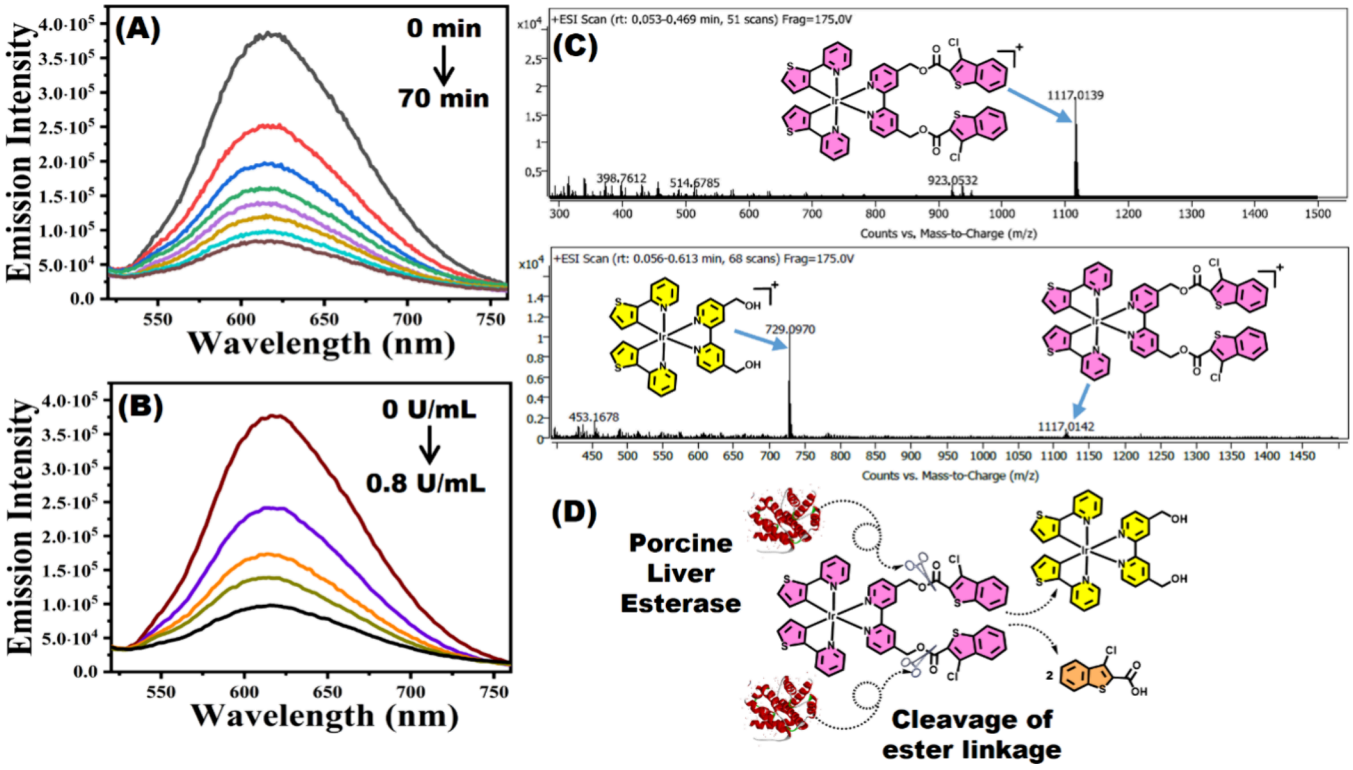

Figure 4. (A) Time-dependent and (B) concentration-dependent changes in fluorescence intensity of IrThpy@L2 (10 μM) after treatment with porcine liver esterase (PLE) at room temperature (λ_{exc}= 405 nm). (C) HRMS spectra of IrThpy@L2 (10 μM) in the absence of PLE (top) and in the presence of PLE (0.2 U/mL) after being incubated for 70 min at room temperature (bottom). (D) Schematic diagram representing the esterase mediated release of IrThpy@OH and I-2 from IrThpy@L2.

spectroscopy studies were performed. The time-dependent fluorescence emission intensity of IrThpy@L2 was measured at 10 min time interval after treatment with PLE (Figure 4A). There was a gradual decrement in the fluorescence intensity suggesting that IrThpy@L2 gets hydrolyzed into IrThpy@OH and I-2 by PLE as the fluorescence intensity of IrThpy@L2 is approximately 8 times greater than that of IrThpy@OH (Figure S35C). A control experiment was conducted to examine the stability of IrThpy@L2 in PBS in the absence of PLE (Figure S35D). There was no noticeable change in the emission intensity of IrThpy@L2 in DMSO/PBS (0.4%) buffer solution even after 70 min, suggesting that the complex is stable in PBS buffer and gets activated only in the presence of esterase.

After that, concentration-dependent fluorescence emission spectra were also recorded in which IrThpy@L2 was treated with different concentrations of PLE with the same time intervals (Figure 4B). With the increase in PLE concentration, the fluorescence emission intensity decreased, which again indicates the hydrolysis of ester bonds to yield cytotoxic species, i.e. IrThpy@OH and I-2 (Figure 4D). Additionally, IrThpy@L2 was incubated with PLE in PBS for 70 min. The HRMS spectra were recorded before and after the PLE treatment. After PLE treatment with IrThpy@L2, it showed m/z peaks designated to the intact complex as well as complex IrThpy@OH (Figure 4C) which further confirms the enzymatic hydrolysis of the lead complex to release the cytotoxic species.

https://doi.org/10.1021/acs.inorgchem.4c03950
Inorg. Chem. 2024, 63, 24709−24723

Cellular Localization Studies. The subcellular localization of IrThpy@L2 in HCT116 cells was studied by using fluorescence microscopy. The fluorescence emission property of IrThpy@L2 was utilized to study its uptake in HCT116 cells; bright red fluorescence emanating from the cells represents significant uptake of IrThpy@L2 in HCT116 cells (Figure 5A). Also, the fluorescence emission of IrThpy@L2 in the red region was utilized to examine its subcellular localization. To perform this study, HCT116 cells were treated with IrThpy@L2 for 30 min and then incubated separately with organelle-specific staining dyes such as Mitotracker Green, Lysotracker Green, and 4′,6-diamidino-2-phenylindole (DAPI). Fluorescence images were further visualized to evaluate the colocalization studies. The colocalization results suggested that the green fluorescence of Mitotracker Green overlapped to a greater extent with the red fluorescence of IrThpy@L2 in the merged channel (appeared as yellow) with Pearson's correlation coefficient of 0.8 (Figure 5B). On the contrary, IrThpy@L2 exhibits poor colocalization for lysosome and nucleus with Pearson's correlation coefficient of 0.3 and 0.2, respectively (Figure 5C, D). These results revealed the maximum accumulation of IrThpy@L2 inside mitochondria rather than lysosomes and nuclei.

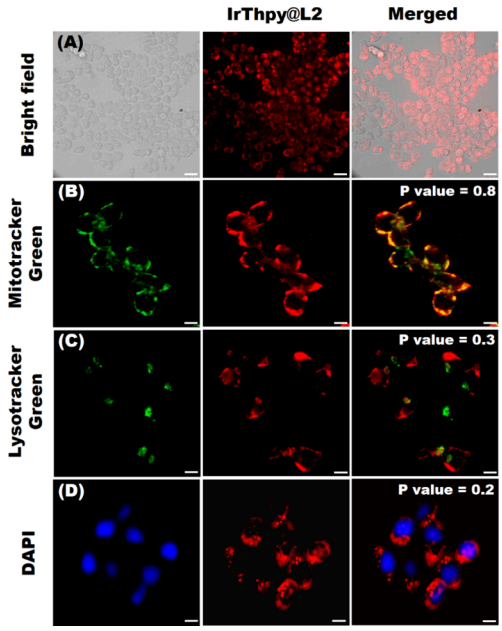

Figure 5. (A) The cellular uptake images of IrThpy@L2 after 1 h incubation with the HCT116 cell line. Magnification: 40x, scale bar: 20 μm. Intracellular localization of IrThpy@L2 in HCT116 cells costained with organelle targeting dye, i.e. Mitotracker Green (ex/em: 490/516 nm) (B), Lysotracker Green (ex/em: 504/511 nm) (C) and DAPI (ex/em: 364/454 nm) (D). Magnification: 60x, scale bar: 10 μm.

Mechanism of Cell Death Investigation. The cytotoxicity result of IrThpy@L2 and prodrug activation studies encouraged us to investigate ROS production and further its implication in the induction of the cell death process. ROS generation by IrThpy@L2 inside cells was determined using the ROS probe, i.e., 2,7-dichlorodihydrofluorescein diacetate (DCFH-DA). Basically, a nonfluorescent cell-permeable dye DCFH-DA gets oxidized to form dichlorofluorescein (DCF) in the presence of ROS, which shows bright green fluorescence.[103] HCT116 cells were treated with IrThpy@L2 and stained with DCFH-DA. H_2O_2-treated cells were used as a positive control. The results revealed that untreated cells exhibited a weak fluorescence emission. Green emission was observed from a few cells for the positive control. Cells treated with IrThpy@L2 showed the highest green fluorescence for DCF (Figure 6A). ROS concentration is directly proportional to the fluorescence intensity of DCF (λ_{em} = 535 nm). So, the fluorescence emission of DCF was quantified using a microplate reader. The result demonstrated that there is about a 7-fold increase in emission intensity of DCF in the presence of IrThpy@L2 when compared with control cells,

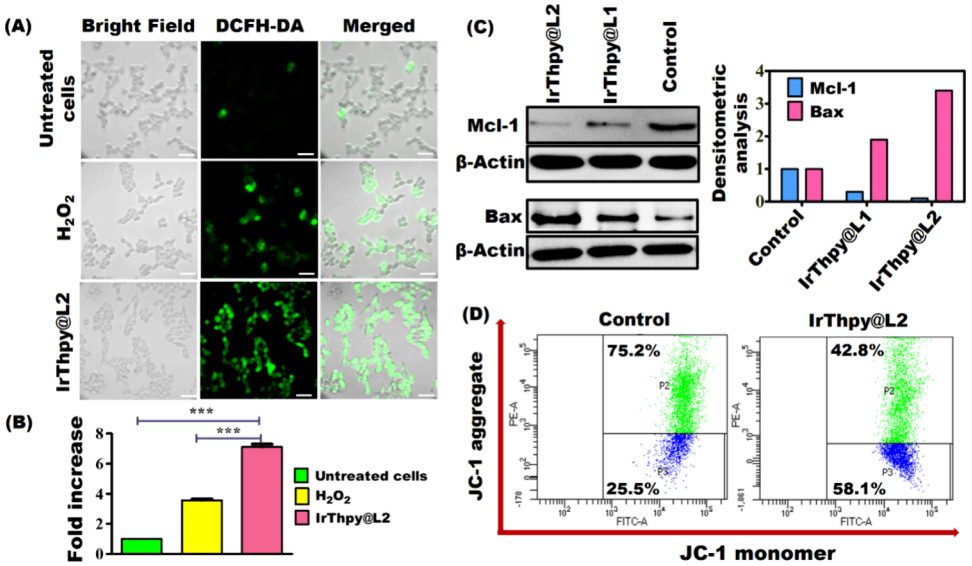

Figure 6. (A) Determination of ROS generation by DCFH-DA in HCT116 cells before and after treatment with IrThpy@L2 and H_2O_2 treated cells as a positive control. Magnification: 40x. scale bar: 20 μm. (B) Corresponding statistical analysis of the generation of ROS in HCT116 cells. One-way ANOVA with Turkey multiple comparison test was used to measure the p values, ***$p < 0.001$, and data expressed as mean ± SD (n = 2). (C) Western blot analysis quantifying different protein expressions using a densitometric plot. (D) Effect of IrThpy@L2 on MMP analyzed by flow cytometry using JC-1 dye.

https://doi.org/10.1021/acs.inorgchem.4c03950
Inorg. Chem. 2024, 63, 24709−24723

confirming the elevated ROS levels (Figure 6B). Therefore, these results clearly signify that the activation of IrThpy@L2 in the presence of mitochondrial esterase releases ROS generator IrThpy@OH[86] which further induces ROS-mediated apoptosis.

To further confirm the activation of prodrug IrThpy@L2, Western blot analysis was conducted to quantify the expression of antiapoptotic Mcl-1 protein and proapoptotic Bax protein. The results indicated the downregulation of Mcl-1 and upregulation of Bax, which further attests to the induction of the apoptosis that proceeds via inhibition of Mcl-1 protein (Figure 6C). Overall, our experimental results validated the esterase mediated activation of prodrug IrThpy@L2 and subsequent release of Mcl-1 inhibitor[15] and IrThpy@OH which induce mitochondrial outer membrane permeabilization (MOMP) resulting in mitochondria-mediated apoptosis by ROS generation and Mcl-1 inhibition (Figure 7).

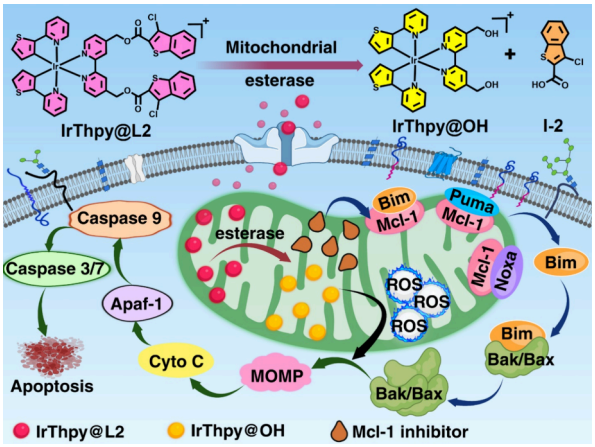

Figure 7. Schematic diagram represents the plausible mechanism of action of synthesized iridium(III) prodrugs.

The induction of cellular apoptosis through mitochondrial dysfunction was evaluated for IrThpy@L2 by measuring the mitochondrial membrane potential (MMP). Mitochondrial dysfunction is visualized using 5,5′,6,6′-tetrachloro-1,1′,3,3′-tetraethylimidacarbocyanine iodide (JC-1). For a healthy polarized mitochondrion, JC-1 emits red fluorescence when it exists in an aggregated form. On the other hand, JC-1 shows green fluorescence when it exists as a monomer in the case of depolarized mitochondria with low MMP.[104]

HCT116 cells treated with IrThpy@L2 showed green fluorescence (Figure S37), representing the loss of mitochondrial integrity. Moreover, red fluorescence is seen for untreated HCT116 cells depicting high MMP due to the JC-1 aggregates. The flow cytometry analysis further showed a higher percentage of IrThpy@L2 treated cells present in the monomeric region (58.1%) as compared to the untreated cells (25.5%) which suggests that IrThpy@L2 causes a significant loss in the mitochondrial membrane potential of HCT116 cells (Figure 6D).

Nuclear deformation and fragmentation studies were performed using nuclear staining dye, DAPI, to investigate the cellular DNA damage process using fluorescence microscopy.[105] IrThpy@L2 treated cells show intense fluorescence for DAPI due to condensed chromatin, thus representing the DNA damage process. Untreated HCT116 cells showed no signs of nuclear fragmentation. However, positive control Cisplatin exhibits bright fluorescence due to its DNA targeting ability. The greater extent of nuclear deformation and disintegration observed for IrThpy@L2 demonstrated that cells were undergoing DNA damage, ultimately leading to apoptosis (Figure 8A).

The lowering of MMP and nuclear fragmentation further encouraged us to analyze the cell cycle progression at 6 h post-treatment with IrThpy@L2 in HCT116 cells. Propidium iodide (PI) staining is utilized to evaluate the cell cycle distribution by using flow cytometry analysis. It shows the distribution of cells in distinct phases of the cell cycle (G0/G1, S, Sub G1, and G2/M) for IrThpy@L2, Cisplatin as a positive control and untreated cells (Figure 8B). The results indicated that IrThpy@L2 is arresting the cell cycle in the S phase compared with untreated cells and Cisplatin. In addition, along with a significant reduction in the G0/G1 phase, there was an increment in cell population in the Sub G1 phase for IrThpy@L2 treated cells. These results demonstrate that complex IrThpy@L2 induced cell death in HCT116 after the disruption of cell cycle progression.

Flow cytometry analysis with Annexin V- fluorescein isothiocyanate (Annexin V-FITC) and propidium iodide (PI) was conducted to determine the extent of cell apoptosis and necrosis in HCT116 cells. For cells incubated with IrThpy@L2, 7.3% and 25.5% of the cell populations were in the early and late apoptosis stages, respectively (Figure 8C). Whereas at a similar concentration of Cisplatin, only 12.1% and 9.4% of cells were in the early and late apoptosis stages, respectively. These results confirmed that the synthesized prodrug could induce cell apoptosis more effectively than Cisplatin.

To further confirm the cytotoxic activity of the prodrug, fluorescein diacetate (FDA) and PI costaining assay were performed for IrThpy@L2 treated HCT116 cells (Figure 8D). FDA (permeable dye) is hydrolyzed by cellular esterase to show intense green fluorescence for live cells. PI (non-permeable dye) emits red fluorescence for dead cells after binding to DNA.[106] The fluorescence microscopic images of HCT116 treated with 5 μM IrThpy@L2 after 6 h showed a decrement in green fluorescence compared to untreated cells. No green fluorescence is observed after 8h of incubation with IrThpy@L2. On the other hand, the proportion of cells stained with PI was significantly higher in the case of IrThpy@L2 treated cells when correlated with the untreated control group. Thus, these results confirmed that IrThpy@L2 has the potential to induce cell death in HCT116 cells.

3D Multicellular Tumor Spheroids Studies. 3D Multicellular tumor spheroids were found to depict the most promising 3D *in vitro* model used to study where the invasive nature of cancer is much related to the *in vivo* model.[107] Moreover, MCTS studies are considered as the perfect *in vitro* model to represent the therapeutic potential of the drug. The images were taken through an inverted microscope and subjected to morphological analysis.

When spheroids were treated with IrThpy@L2, the loss in the solidity of MCTS and disintegration was witnessed, compared with the untreated (control) MCTS (Figure 9A). The compact perimeter in the case of untreated spheroids was destroyed for IrThpy@L2 treated spheroids after 6 days, which indicated the cytotoxic potential of IrThpy@L2 against HCT116 MCTS. Furthermore, to confirm the cell death activity in MCTS, fluorescence microscopic analysis of live/dead cell staining was performed using FDA (for live cells) and PI (for dead cells). The images were visualized in the green

https://doi.org/10.1021/acs.inorgchem.4c03950
Inorg. Chem. 2024, 63, 24709−24723

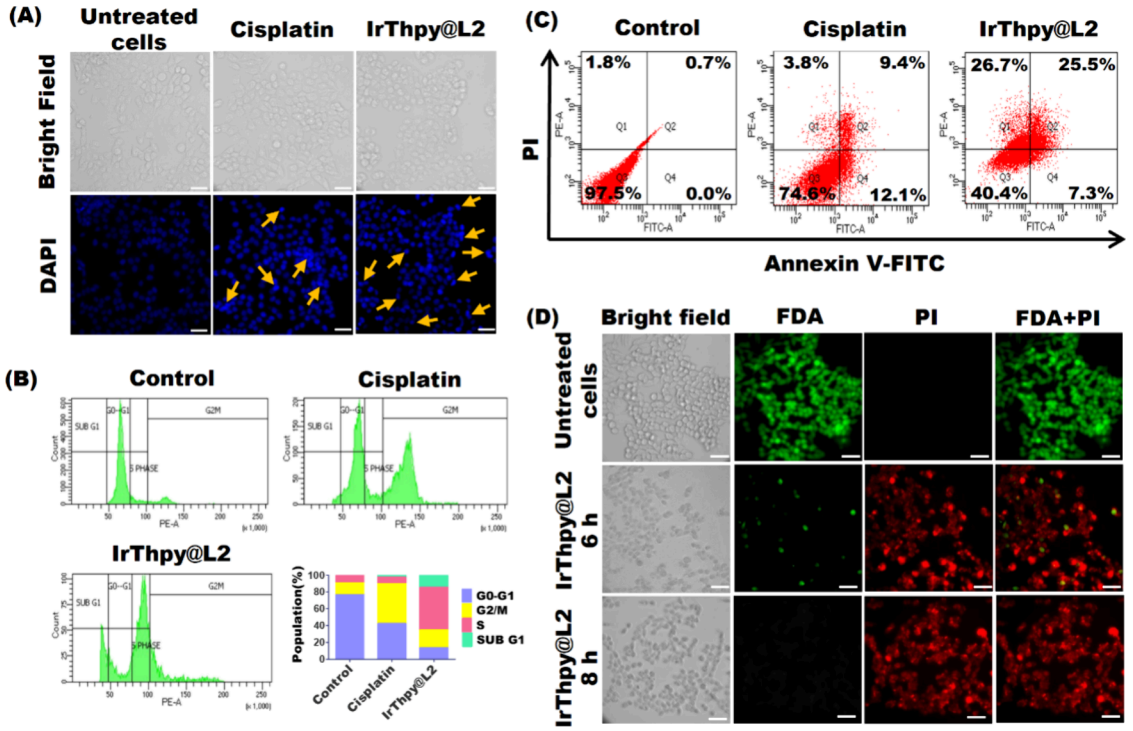

Figure 8. (A) Nuclear fragmentation of HCT116 cells treated with IrThpy@L2 followed by DAPI staining. Magnification: 40x, scale bar: 20 μm. (Arrow represents condensation of DNA inside the nucleus). (B) Histogram profile of HCT116 in various stages of the cell cycle with stacked bar graph represents the cell percentage in each phase of the cell cycle after 6 h of treatment with IrThpy@L2 at 5 μM concentration. The subG1 cell population represents apoptotic/necrotic cells. (C) Quantification of apoptotic HCT116 cells using flow cytometric analysis data of cells stained with Annexin V-FITC and PI. (D) FDA/PI costaining for HCT116 cells for untreated cells and IrThpy@L2 treated cells after 6 and 8 h. (Green fluorescence depicts viable cells, and red fluorescence indicates dead cells). Magnification: 40x, scale bar: 20 μm.

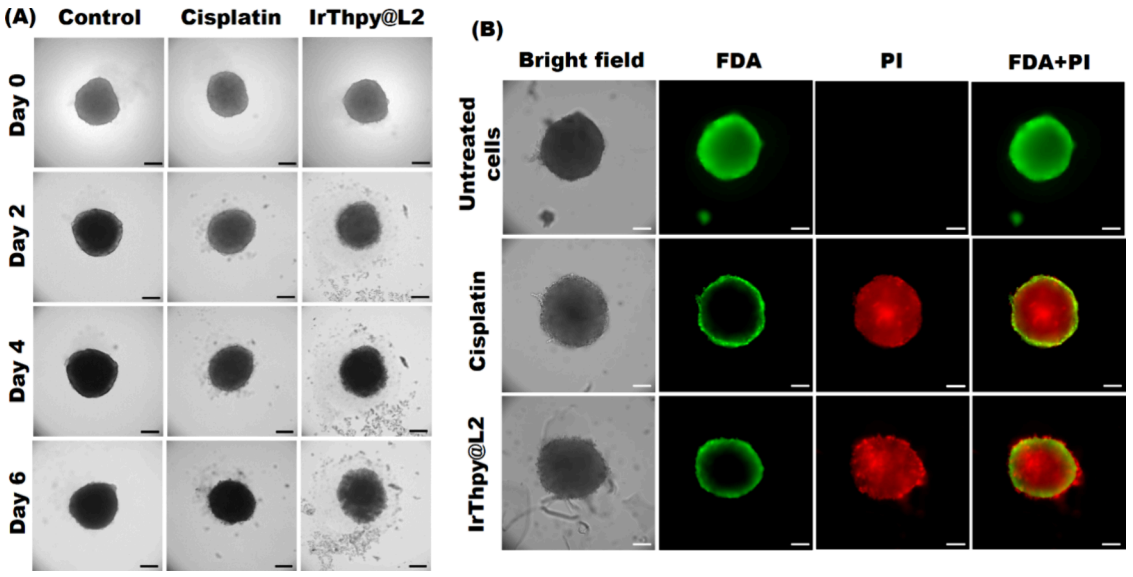

Figure 9. (A) Morphology changes in HCT116 MCTS after incubation with IrThpy@L2 (5 μM) and Cisplatin (50 μM). (B) Fluorescence microscope images of live/dead cells in HCT116 MCTS after FDA/PI staining. Magnification: 10×, scale bar: 100 μm.

channel (for FDA) and red channel (for PI) after 48 h of treatment with IrThpy@L2. Fewer cells stained in green channels were observed for IrThpy@L2 treated cells compared with untreated control groups (Figure 9B). In addition to this, cells stained with PI in the red channel were remarkably higher for IrThpy@L2 (5 μM) treated MCTS. Similar observation was noted for positive control Cisplatin (50 μM) treated MCTS at higher concentrations. These results confirmed that IrThpy@L2 is capable of effectively inducing apoptosis in the MCTS.

CONCLUSIONS

In summary, we synthesized six cyclometalated iridium(III) prodrugs bearing Mcl-1 inhibitors. Among them, IrThpy@L2 exhibited excellent cytotoxicity against the HCT116 cancer cell line, which was approximately 600 times more potent than

https://doi.org/10.1021/acs.inorgchem.4c03950
Inorg. Chem. 2024, 63, 24709−24723

Cisplatin. Most notably, IrThpy@L2 was found to be more selective towards cancer cells as compared to normal human hepatic cells (WRL-68). Uptake studies suggest that IrThpy@L2 effectively internalizes in the HCT116 cell line and substantially localizes in the mitochondria. Furthermore, PLE mediated activation of IrThpy@L2 was evident from fluorescence emission and HRMS studies. Western blotting analysis was performed to understand the mitochondrial esterase mediated activation of IrThpy@L2. The generation of ROS, MMP depolarization, downregulation of Mcl-1 protein, and upregulation of Bax protein further attest the activation of IrThpy@L2 in the HCT116 cell line due to the overexpression of mitochondrial esterase. Furthermore, the activity of IrThpy@L2 was also tested against 3D multicellular tumor spheroids (MCTS) to mimic the solid tumor microenvironment. Our work signifies that incorporation of Mcl-1 inhibitors into the iridium(III) complex not only improves its anticancer activity but also imparts targeting ability. This strategy can be further exploited to design targeted multifunctional prodrugs by conjugating metal complexes with other bioactive molecules/drugs to open new avenues for futuristic anticancer therapies.

EXPERIMENTAL SECTION

General Materials and Methods. All starting materials, reagents, and solvents were purchased from commercial vendors and used without any further purification. Column chromatography was performed using silica gel (100−200 mesh). Iridium(III)chloride hydrate, MitoTracker Green FM, LysoTracker Green DND-26, (3-(4,5-dimethylthiazol-2-yl)-2,5-diphenyltetrazolium bromide (MTT), JC-1 assay kit, FITC Annexin V/Dead Cell Apoptosis Kit and Fetal bovine serum (FBS) were purchased from Thermo Fisher Scientific. 2-Phenylpyridine, Porcine liver esterase (PLE), 2′,7′-dichlorofluorescein diacetate (DCFH-DA), 4′,6-diamidino-2-phenylindole (DAPI) and Fluorescein diacetate (FDA) were purchased from Sigma-Aldrich. Dulbecco's modified Eagle's medium (DMEM), Roswell Park Memorial Institute medium 1640 (RPMI 1640) and cell-lysis RIPA buffer were purchased from HIMEDIA. 4,4′-Dimethyl-2,2′-bipyridyl, 5-Chloroindole-2-carboxylic acid were purchased from TCI. Antibodies Mcl-1, Bax for Western blot were purchased from Cloud-Clone Corp. and β-actin was purchased from Bio-Rad. Propidium iodide was purchased from SRL. Benzo[h]quinoline, 2-(Thiophen-2-yl)pyridine and 3-Chlorobenzo[b]thiophene-2-carboxylic acid were purchased from BLD Pharma India. Deuterated solvents, such as DMSO-d_6 (dimethyl sulfoxide) and $CDCl_3$ (chloroform), were purchased from Eurisotop. All the experiments were performed using deionized water wherever required. The rest of the chemicals were all analytical grade and obtained from commercial sources.

The cyclometalated iridium(III) chloro-bridged dimers $[(ppy)_2\text{-Ir-}\mu\text{-Cl}]_2$, $[(bzq)_2\text{-Ir-}\mu\text{-Cl}]_2$, and $[(thpy)_2\text{-Ir-}\mu\text{-Cl}]_2$ were prepared according to the previous literature methods.[87] All of the synthesized complexes were characterized by ^{1}H NMR, ^{13}C NMR, and HRMS spectrometry. All the complexes were dissolved in DMSO before performing the biological experiments and the concentration of DMSO was 0.4% vol in DMEM with 10% FBS.

General Instrumentation. Nuclear magnetic resonance spectra (NMR) were recorded by a JEOL-500 MHz spectrometer (^{1}H NMR: 500 MHz, ^{13}C NMR: 126 MHz) using DMSO-d_6 and $CDCl_3$ as the deuterated solvent. High-resolution mass spectra (HRMS) were recorded in Agilent 6545 LC/Q-TOF mass spectrometer. UV−visible absorption spectra were recorded on Shimadzu UV-2600 UV/vis/NIR spectrophotometer. The emission spectra were recorded using Horiba Fluoromax spectrophotometer. The MTT and quantification of DCFH-DA assays were performed with the help of SYNERGY H1 microplate reader.

General Synthetic Procedures for Ligands (L1 and L2) and Ir(III) Complexes. *Ligands L1 and L2.* As shown in Figure S1(e), 2-5 was prepared according to a previous reported literature.[88] After that, Cs_2CO_3 (5.84 mmol, 4 equiv) was suspended in dry DMF at 0 °C, then I-1/I-2 (2.92 mmol, 2 equiv) were added at the same temperature. Then 5 (1.46 mmol) was added in portions, and the reaction mixture was shifted to room temperature (30 °C). The reaction mixture was further allowed to stir at room temperature for 12 h. After completion of the reaction, the product precipitated out was washed with water and further used for complex synthesis without further purification.

Ligand L1. Off-white solid (Yield 97%). ^{1}H NMR (500 MHz, DMSO-d_6) δ 12.25 (s, 2H), 8.71 (d, J = 5.0 Hz, 2H), 8.47 (s, 2H), 7.77 (d, J = 2.1 Hz, 2H), 7.57 (dd, J = 5.0, 1.4 Hz, 2H), 7.49 (dd, J = 8.8, 0.6 Hz, 2H), 7.31−7.27 (m, 4H), 5.55 (s, 4H); ^{13}C NMR (126 MHz, DMSO-d_6) δ 160.71, 155.25, 149.71, 146.54, 136.00, 128.06, 127.75, 125.18, 124.89, 122.51, 121.28, 118.67, 114.40, 108.10, 64.55. HRMS (ESI): m/z calculated for $[M + H]^+$: 571.0862. Found: 571.0962.

Ligand L2. Off-white solid (Yield 95%). ^{1}H NMR (500 MHz, DMSO-d_6) 8.74 (d, J = 5.0 Hz, 2H), 8.54 (s, 2H), 8.17 (d, J = 8.1 Hz, 2H), 8.01 (d, J = 7.7 Hz, 2H), 7.66 (m, J = 26.1, 8.1, 7.1, 1.1 Hz, 4H), 7.57 (d, J = 3.5 Hz, 2H), 5.59 (s, 4H); ^{13}C NMR (126 MHz, DMSO-d_6) δ 160.18, 155.27, 149.78, 146.06, 138.12, 136.26, 129.08, 126.60, 126.42, 125.25, 123.76, 123.51, 122.48, 118.74, 65.55. HRMS (ESI): m/z calculated for $[M + H]^+$: 605.0085. Found: 605.0177.

General Procedure for the Synthesis of Iridium(III) Prodrugs. As shown in Figure 1A, IrPpy@L1, IrPpy@L2, IrBzq@L1, IrBzq@L2, IrThpy@L1, and IrThpy@L2 were prepared by adding a solution of appropriate Ir(III) chloro-bridged dimer in DCM (10 mL) into the solution of ligand L1/L2 (2.1 equiv) in DMF (5 mL) and the reaction mixture was stirred for 12 h at 70 °C under the nitrogen atmosphere, followed by anion exchange with saturated NH_4PF_6 solution in methanol (5 mL) for 2 h. The desired product was achieved after purification by silica gel column chromatography (5:95 v/v Methanol/DCM).

General Procedure for the Synthesis of Reference Complexes. Complexes IrPpy@OH, IrBzq@OH, IrThpy@OH were synthesized using similar strategy as mentioned above with a slight modification in the synthetic procedure by using a methanolic solution of 4 in place of L1/L2. Briefly, a solution of appropriate Ir(III) chloro-bridged dimer in DCM (10 mL) was added into the methanolic solution of ligand 4 (2.1 equiv) (10 mL) and the reaction mixture was stirred for 12 h at 60 °C under the nitrogen atmosphere, followed by anion exchange with saturated NH_4PF_6 solution in methanol (5 mL) for 2 h. The desired product was achieved after purification via silica gel column chromatography in CH_2Cl_2/CH_3OH.

Complex IrPpy@L1. Bright yellow solid (Yield 45%). ^{1}H NMR (500 MHz, DMSO-d_6) δ 12.20 (s, 2H), 8.98 (s, 2H), 8.26 (d, J = 8.2 Hz, 2H), 7.95−7.86 (m, 8H), 7.68 (d, J = 5.1 Hz, 4H), 7.46 (d, J = 8.8 Hz, 2H), 7.33−7.23 (m, 4H), 7.17 (t, J = 6.2 Hz, 2H), 7.03 (t, J = 7.4 Hz, 2H), 6.91 (t, J = 7.5 Hz, 2H), 6.20 (d, J = 7.5 Hz, 2H), 5.62 (s, 4H); ^{13}C NMR (126 MHz, DMSO-d_6) δ 166.89, 160.49, 155.24, 150.37, 150.09, 149.15, 149.02, 143.87, 138.95, 136.02, 131.14, 130.37, 127.83, 127.70, 126.69, 125.29, 125.18, 124.95, 124.04, 123.11, 122.43, 121.20, 120.17, 114.35, 108.50, 63.98. HRMS (ESI): m/z calculated for $[M\text{-}PF_6]^+$: 1071.1804. Found: 1071.1806.

Complex IrPpy@L2. Bright yellow solid (Yield 47%). ^{1}H NMR (500 MHz, DMSO-d_6) δ 8.93 (s, 2H), 8.28 (d, J = 8.2 Hz, 2H), 8.08 (d, J = 8.2 Hz, 2H), 7.97−7.91 (m, 8H), 7.82 (d, J = 4.8 Hz, 2H), 7.64 (ddd, J = 30.4, 15.8, 6.5 Hz, 6H), 7.18 (t, J = 6.1 Hz, 2H), 7.03 (t, J = 7.5 Hz, 2H), 6.91 (td, J = 7.6, 1.0 Hz, 2H), 6.19 (d, J = 7.3 Hz, 2H), 5.68 (s, 4H); ^{13}C NMR (126 MHz, DMSO-d_6) δ 166.81, 159.97, 155.21, 150.21, 150.17, 149.02, 148.72, 143.81, 138.87, 138.08, 136.08, 131.07, 130.28, 129.01, 126.73, 126.48, 126.28, 125.12, 125.00, 123.98, 123.53, 123.34, 122.78, 122.35, 120.10, 64.76. HRMS (ESI): m/z calculated for $[M\text{-}PF_6]^+$: 1105.1028. Found: 1105.1030.

Complex IrBzq@L1. Yellow solid (Yield 41%). ^{1}H NMR (500 MHz, DMSO-d_6) δ 12.18 (s, 2H), 9.03 (s, 2H), 8.59 (d, J = 7.5 Hz, 2H), 8.18−8.14 (m, 2H), 7.98 (d, J = 8.9 Hz, 2H), 7.88 (dd, J = 14.2, 7.3 Hz, 4H), 7.78 (d, J = 5.2 Hz, 2H), 7.67 (d, J = 1.8 Hz, 2H), 7.62

https://doi.org/10.1021/acs.inorgchem.4c03950
Inorg. Chem. 2024, 63, 24709−24723

(dd, J = 8.1, 5.5 Hz, 2H), 7.56 (d, J = 7.9 Hz, 2H), 7.44 (d, J = 8.8 Hz, 2H), 7.30−7.25 (m, 4H), 7.19 (t, J = 7.6 Hz, 2H), 6.24 (d, J = 7.1 Hz, 2H), 5.61 (s, 4H); ^{13}C NMR (126 MHz, DMSO-d_6) δ 161.71, 157.58, 156.86, 151.86, 150.40, 150.04, 148.43, 141.43, 139.05, 137.24, 135.09, 131.07, 130.85, 129.75, 129.04, 128.91, 128.07, 127.93, 126.51, 126.16, 125.55, 124.37, 124.18, 122.42, 121.66, 115.59, 109.69, 64.37. HRMS (ESI): m/z calculated for $[M\text{-}PF_6]^+$: 1119.1804. Found: 1119.1842.

Complex IrBzq@L2. Yellow solid (Yield 40%). ^{1}H NMR (500 MHz, DMSO-d_6) δ 8.97 (s, 2H), 8.59 (dd, J = 8.1, 0.9 Hz, 2H), 8.17 (dd, J = 5.4, 1.0 Hz, 2H), 8.06 (d, J = 8.1 Hz, 2H), 7.98 (d, J = 8.9 Hz, 2H), 7.92−7.88 (m, 6H), 7.71 (d, J = 5.6 Hz, 2H), 7.66−7.54 (m, 8H), 7.18 (t, J = 7.6 Hz, 2H), 6.22 (d, J = 7.0 Hz, 2H), 5.67 (s, 4H); ^{13}C NMR (126 MHz, DMSO-d_6) δ 160.01, 156.31, 155.62, 150.84, 148.85, 148.77, 147.06, 140.17, 138.11, 137.78, 136.10, 133.81, 129.81, 129.59, 129.07, 128.47, 126.81, 126.78, 126.52, 126.33, 125.01, 124.29, 123.58, 123.39, 122.94, 122.78, 120.40, 64.79. HRMS (ESI): m/z calculated for $[M\text{-}PF_6]^+$: 1153.1028. Found: 1153.1049.

Complex IrThpy@L1. Brown solid (Yield 49%). ^{1}H NMR (500 MHz, DMSO-d_6) δ 12.20 (s, 2H), 8.98 (s, 2H), 7.93 (dd, J = 5.8, 1.6 Hz, 2H), 7.87 (d, J = 5.7 Hz, 2H), 7.82 (ddd, J = 8.2, 7.4, 1.4 Hz, 2H), 7.77 (ddd, J = 8.2, 1.5, 0.8 Hz, 2H), 7.70 (d, J = 2.1 Hz, 2H), 7.67 (d, J = 4.7 Hz, 2H), 7.61−7.58 (m, 2H), 7.48−7.45 (m, 2H), 7.33 (dd, J = 2.2, 0.9 Hz, 2H), 7.28 (dd, J = 8.8, 2.1 Hz, 2H), 6.98 (ddd, J = 7.4, 5.9, 1.6 Hz, 2H), 6.19 (d, J = 4.7 Hz, 2H), 5.64 (s, 4H); ^{13}C NMR (126 MHz, DMSO-d_6) δ 163.14, 160.64, 155.54, 152.51, 150.86, 149.71, 149.43, 139.66, 136.41, 136.18, 131.26, 130.51, 127.98, 127.84, 126.96, 125.44, 125.09, 123.23, 121.36, 121.29, 118.59, 114.53, 108.64, 64.11. HRMS (ESI): m/z calculated for $[M\text{-}PF_6]^+$: 1083.0933. Found: 1083.0964.

Complex IrThpy@L2. Brown solid (Yield 44%). ^{1}H NMR (500 MHz, DMSO-d_6) δ 8.92 (s, 2H), 8.10−8.07 (m, 2H), 7.93−7.90 (m, 2H), 7.89 (d, J = 5.7 Hz, 2H), 7.86−7.83 (m, 2H), 7.82−7.80 (m, 2H), 7.77 (ddd, J = 8.2, 1.4, 0.8 Hz, 2H), 7.67−7.64 (m, 4H), 7.62−7.58 (m, 4H), 6.98 (ddd, J = 7.4, 5.9, 1.5 Hz, 2H), 6.19−6.16 (m, 2H), 5.69 (s, 4H); ^{13}C NMR (126 MHz, DMSO-d_6) δ 163.34, 160.46, 155.79, 152.54, 151.20, 149.95, 149.27, 139.89, 138.47, 136.63, 136.48, 131.41, 130.72, 129.48, 127.20, 126.99, 126.74, 125.36, 123.91, 123.77, 123.05, 121.51, 118.78, 65.18. HRMS (ESI): m/z calculated for $[M\text{-}PF_6]^+$: 1117.0156. Found: 1117.0159.

Complex IrPpy@OH. Bright yellow solid (Yield 81%). ^{1}H NMR (500 MHz, $CDCl_3$) δ 9.04 (s, 2H), 7.89 (d, J = 8.2 Hz, 2H), 7.79−7.65 (m, 8H), 7.50 (d, J = 5.5 Hz, 2H), 7.37 (d, J = 5.5 Hz, 2H), 7.03−6.99 (m, 4H), 6.90 (t, J = 7.4 Hz, 2H), 6.29 (d, J = 7.6 Hz, 2H), 4.91 (s, 4H); ^{13}C NMR (126 MHz, DMSO-d_6) δ 163.04, 156.22, 155.23, 152.67, 149.98, 149.31, 139.33, 136.14, 131.57, 130.95, 130.41, 128.70, 125.80, 121.74, 121.02, 118.31, 61.28. HRMS (ESI): m/z calculated for $[M\text{-}PF_6]^+$: 717.1841. Found: 717.1861.

Complex IrBzq@OH. Yellow solid (Yield 85%). ^{1}H NMR (500 MHz, DMSO-d_6) δ 8.78 (s, 2H), 8.58 (d, J = 7.9 Hz, 2H), 8.09 (d, J = 5.1 Hz, 2H), 7.98 (d, J = 8.8 Hz, 2H), 7.89 (d, J = 8.9 Hz, 2H), 7.76 (d, J = 5.7 Hz, 2H), 7.61 (dd, J = 8.0, 5.5 Hz, 2H), 7.54 (dd, J = 12.4, 6.7 Hz, 4H), 7.18 (t, J = 7.6 Hz, 2H), 6.22 (d, J = 7.1 Hz, 2H), 5.78 (t, J = 5.5 Hz, 2H), 4.74 (d, J = 5.4 Hz, 4H); ^{13}C NMR (126 MHz, DMSO-d_6) δ 166.96, 156.07, 155.14, 150.75, 149.43, 148.83, 143.89, 138.81, 131.19, 130.32, 128.99, 128.30, 125.71, 125.15, 123.96, 122.30, 121.80, 120.09, 61.35. HRMS (ESI): m/z calculated for $[M\text{-}PF_6]^+$: 765.1841. Found: 765.1844.

Complex IrThpy@OH. Brown solid (Yield 80%). ^{1}H NMR (500 MHz, DMSO-d_6) δ 8.73 (s, 2H), 7.81 (t, J = 7.6 Hz, 2H), 7.78−7.74 (m, 4H), 7.68−7.64 (m, 4H), 7.53 (d, J = 5.6 Hz, 2H), 6.96 (t, J = 6.5 Hz, 2H), 6.18 (d, J = 4.7 Hz, 2H), 5.81 (t, J = 5.5 Hz, 2H), 4.77 (d, J = 5.3 Hz, 4H); ^{13}C NMR (126 MHz, DMSO-d_6) δ 163.22, 156.37, 155.41, 152.85, 150.17, 149.49, 139.51, 136.31, 131.13, 130.59, 125.98, 121.90, 121.19, 118.49, 61.46. HRMS (ESI): m/z calculated for $[M\text{-}PF_6]^+$: 729.0970. Found: 729.0974.

Crystallographic Structure Determination. A specimen of $C_{52}H_{34}Cl_2IrN_4O_4S_2$, approximate dimensions 0.034 × 0.106 × 0.227 mm, was used for the X-ray crystallographic analysis, and the measurements were performed on a Bruker APEX-II CCD diffractometer (Mo Kα λ = 0.71073). The total exposure time was 4.92 h. The frames were integrated with the Bruker SAINT software package using a narrow-frame algorithm. The integration of the data using a monoclinic unit cell yielded a total of 227513 reflections to a maximum θ angle of 26.43° (0.80 Å resolution), of which 12237 were independent (average redundancy 18.592, completeness = 99.3%, R_{int} = 5.88%, R_{sig} = 3.45%) and 10661 (87.12%) were greater than $2\sigma(F^2)$. The final cell constants of a = 14.2102(14) Å, b = 30.898(3) Å, c = 14.9071(15) Å, α = 90°, β = 113.649(3)°, γ = 90°, volume = 5995.5(10) Å^3, are based upon the refinement of the XYZ-centroids of 9733 reflections above 20 σ(I) with 4.954° < 2θ < 50.38°. Data were corrected for absorption effects using the Multi-Scan method (TWINABS). The ratio of minimum to maximum apparent transmission was 0.609. The calculated minimum and maximum transmission coefficients (based on crystal size) are 0.6090 and 0.9220. The structure was solved and refined using the Bruker SHELXTL Software Package, using space group P 1 21/c 1, with Z = 4 for the formula unit, $C_{52}H_{34}Cl_2IrN_4O_4S_2$. The final anisotropic full-matrix least-squares refinement on F^2 with 614 variables converged at R1 = 6.56% for the observed data and wR2 = 15.69% for all data. The goodness-of-fit was 1.121. The largest peak in the final difference electron density synthesis was 2.324 e$^-$/Å^3 and the largest hole was −1.301 e$^-$/Å^3 with an RMS deviation of 0.135 e$^-$/Å^3. On the basis of the final model, the calculated density was 1.225 g/cm^3 and F(000), 2196 e$^-$. Crystal data, data collection parameters, and structure refinement details are given in Table S1. Selected bond distances and angles are given in Table S2. CCDC 2310258 (IrPpy@L2).

Hydrolysis of IrThpy@L2 by PLE *in Vitro*. *Time and Concentration Dependent Emission Spectra.* IrThpy@L2 (10 μM) was freshly prepared in 3 mL of PBS, and then a suspension of porcine liver esterase (PLE) (0.2 U/mL) in PBS was added. Time dependent emission spectra were recorded after every 10 min. Similarly, concentration dependent emission spectra were recorded by changing the concentration of PLE from 0.2 to 0.8 U/mL after 10 min incubation.

HRMS. IrThpy@L2 (10 μM) was freshly prepared in 3 mL of PBS, and then a suspension of porcine liver esterase (PLE) (0.2 U/mL) in PBS was added. After the mixture was incubated at 298 K for 70 min, acetone (ice cold) was added to quench the hydrolysis. The sample was centrifuged, and the supernatant was collected and analyzed by HRMS.

Determination of Lipophilicity. The lipophilicity of the complexes was measured in an octanol−water system using the shake flask method. Solutions of IrPpy@L1, IrPpy@L2, IrBzq@L1, IrBzq@L2, IrThpy@L1, and IrThpy@L2 were prepared in an aqueous phase at a concentration of 10 μM. Equal volumes of the solution and 1-octanol saturated with H_2O were mixed and placed in an orbital shaker overnight at 500 rpm. The samples were separated into 2 phases after centrifugation at 8000 rpm for 10 min. Then the concentrations of the complexes in both phases were determined by UV−vis. absorbance. The lipo-hydro partition coefficient Log $P_{o/w}$ were calculated using the following formula:

$P_{o/w} = C_o/C_w = A_o/A_w$ (A stands for absorbance)

Cell Lines and Culture. Human hepatic cells (WRL-68), HeLa (human cervical cancer), HCT116 (human colon cancer), A549 (human pulmonary carcinoma), and HepG2 (human liver cancer) cell lines were purchased from the National Centre for Cell Science (NCCS), Pune, India. Dulbecco's modified eagle medium (DMEM) with fetal bovine serum (FBS, 10%), penicillin G (100 units/mL), sodium bicarbonate (2.2 g/L), and streptomycin (100 mg/mL) is used to grow the cells. Cells were cultured at approximately 80% confluence and kept in a humified incubator at 37 °C with 5% CO_2 in cell culture flasks (tissue cultured) with different sizes depending on the type of experiments to be performed.

ICP-MS Analysis for Cellular Uptake Studies. The cellular accumulation of iridium(III) prodrugs in HCT116 cells was analyzed by ICP-MS. The concentration of iridium for each sample was determined using an Agilent 8900 ICP-MS Triple Quad. Briefly, 7 × 10^4 HCT116 cells were seeded onto a tissue-cultured 12-well plate for 24 h. Then, cells were treated with 5 μM Ir(III) prodrugs for 1 h.

https://doi.org/10.1021/acs.inorgchem.4c03950
Inorg. Chem. 2024, 63, 24709−24723

After the incubation, cells were washed with PBS, trypsinized, and collected. Cells were then digested with 68% of HNO_3 (200 μL) for 24 h at room temperature. The sample solutions were further diluted to a final volume of 10 mL with distilled water and then proceeded for ICP-MS.

Fluorescence Imaging. For cellular uptake imaging studies, 7×10^4 cells were grown over the coverslip in a 6-well plate for 24 h in media with 10% FBS. The cells were treated with 5 μM of IrThpy@L2 for 1 h. After completion of the incubation time, cells were washed carefully with PBS twice to remove excess compound and then coverslips were mounted over the glass slides for fluorescence imaging. All of the imaging experiments were performed using an Olympus fluorescence microscope under different channels. Images were analyzed by using Fiji ImageJ software.

Intracellular Localization. HCT116 cells (7×10^4 cells per well) were seeded onto 6 well plates and incubated with IrThpy@L2 (5 μM) for 30 min in DMEM media. After this, cells were washed with PBS and incubated with Lysotracker Green (300 nM), Mitotracker Green (300 nM), and DAPI (1 μg/mL) separately for 30 min in the dark inside the incubator. Cells were washed thoroughly with PBS, and images were taken with the help of a fluorescence microscope. The images obtained were visualized with Fiji ImageJ software. The value of Pearson's correlation coefficient was determined using the Coloc2 plugin with a scatter plot.

Cytotoxicity Assay. The cell viability or MTT assay was performed using 3-(4,5-dimethylthiazolyl-2)-2,5-diphenyltetrazolium bromide (MTT) dye. The cytotoxicity was examined in the HCT116, HeLa, WRL-68, A549, and HepG2 cell lines. Briefly, 1×10^4 cells per well were cultured in 96 well plates and grown for 24 h in complete media in a humidified incubator with 5% CO_2. The stock solutions of iridium(III) prodrugs (12 mM) and inhibitors (12 mM) were prepared in DMSO and further diluted with media (with 10% FBS) so that the final concentration of DMSO in all the wells was lower than 0.5%. Cells were further treated with different concentrations (5, 15, 30, 50 μM) of prodrugs and inhibitors for 48 h in media. FDA-approved drug, i.e., Cisplatin, was used as a positive control. After incubation, cells were carefully washed with PBS to remove the media. Cells were loaded with a freshly prepared MTT solution (5 mg/mL) for 4 h at 37 °C in the incubator. After 4 h, the formazan crystals (for active cells) were dissolved in 150 μL of DMSO. Finally, the absorbance was measured at 570 nm using a microplate reader. The cell viability was determined by comparing the absorbance of drug-treated cells to that of the cells alone. All experiments were examined in three independent tests (n = 3) and represented as the mean ± standard deviation.

ROS Generation in HCT116 Cell Line. Intracellular ROS levels were detected and quantified using DCFH-DA. Briefly, 7×10^4 HCT116 cells per well were seeded in 6 well plates for 24 h in media. H_2O_2 (working concentration= 50 μM) was taken as a positive control. The cells were treated with 5 μM of IrThpy@L2 and incubated for 2 h at 37 °C in a humidified incubator with 5% CO_2. Cells were carefully washed with 1 mL of PBS and then subjected to DCFH-DA (20 μM) staining at 37 °C for 20 min under dark condition. Cells were then washed with PBS twice, and images were taken under green channels with the help of a fluorescence microscope. All of the images were obtained at the same exposure time. After this, cells were trypsinized, collected by centrifugation, and further dissolved in PBS. The fluorescence intensity of DCF in each group was quantified using a microplate reader with excitation and emission wavelengths of 485 and 535 nm, respectively. The results were plotted as a fold increase in ROS generation by H_2O_2 and IrThpy@L2 correlated with the relative fluorescence of DCF with three independent experiments with $n = 2$ replicates.

Nuclear Fragmentation Assay. For DAPI staining, 7×10^4 HCT116 cells were seeded onto six-well plates and grown for 24 h in a complete media. Cells were further treated with 5 μM IrThpy@L2 for 6 h. Cisplatin (50 μM) was taken as positive control. Cells were carefully washed with PBS and then fixed with 4% freshly prepared paraformaldehyde and kept inside the incubator for 10−15 min. Cells were washed again with PBS and permeabilized by 0.1% TritonX100 for 10−15 min inside incubator. Then the cells were washed with PBS and incubated with DAPI (1 μg/mL) for 30 min in the dark. After that, cells were washed twice with PBS. DAPI-stained images of cells were obtained with the help of a fluorescence microscope under a blue channel.

JC-1 Staining. HCT116 cells with a density of 7×10^4 cells per well were seeded onto six-well plates and allowed to grow for 24 h. Cells were treated with IrThpy@L2 (5 μM) for 4 h. After this period, cells were washed with PBS and stained with JC-1 (5 μg/mL) for 30 min under dark conditions. Cells were thoroughly washed with PBS twice, and images were captured by keeping the exposure time constant.

JC-1 Flow Cytometric Analysis. HCT116 cells were seeded onto a six-well plate with a density of 1×10^5 cells per well for 24 h and then treated with 5 μM of IrThpy@L2 for 4 h. Post treatment, cells were trypsinized and carefully harvested to make cell pellets by centrifugation. Each cell pellet was resuspended in 0.2 mL working solution of JC-1 dye (5 μg/mL) and incubated for 30 min. Then, cells were washed carefully with PBS twice and resuspended in PBS, and immediately flow cytometric analysis was performed using BD FACS instrument, and data was analyzed by BD FACSDiva v8 software.

Western Blotting. HCT116 cells were seeded into six-well plates and incubated under a 5% CO_2 incubator for 24 h. After that, the cells were treated with the control and IrThpy@L2 (1 μM) for 12 h. Then, cells were harvested after trypsinization and lysed in the RIPA lysis buffer. The lysates of all groups obtained were centrifuged at 12000 rpm at 4 °C for 10 min, and the supernatant was collected. Protein samples were separated on SDS-PAGE gel and onto PVDF membranes. The membranes were blocked with 5% freshly prepared skim milk for 1 h at room temperature and then incubated with primary antibody and secondary antibody, respectively. The targeted proteins were detected with a chemiluminescent substrate. Gel Doc was used to visualize the band intensity, which was further quantified using ImageJ software.

Cell Cycle Assay. Using PI staining, analysis of various stages of the cell cycle were analyzed for IrThpy@L2. In brief, HCT116 cells (1×10^5 cells per well) were incubated with IrThpy@L2 (5 μM) and Cisplatin (50 μM) for 6 h. After that, the treated cells were washed with PBS, trypsinized, and harvested by centrifugation. The pellets were carefully washed with ice-cold PBS, fixed with 70% ethanol, and incubated for 2 h at 4 °C. After that, 100 μL of RNase (100 μg/mL) and PI (50 μg/mL) were simultaneously added, and flow cytometry was performed.

Annexin V-FITC/PI Assay. HCT116 cells with a density of 1×10^5 cells per well were seeded in 6 well plates and then incubated with 5 μM of IrThpy@L2 for 6 h. Cells were carefully washed with PBS, trypsinized, and harvested through centrifugation. Cells were washed twice with ice-cold PBS and resuspended in 100 μL of 1x binding buffer. Then, 5 μL of Annexin V-FITC and 5 μL of PI solution were added, and samples were incubated for 15 min in the dark. Finally, flow cytometric analysis was performed.

FDA/PI Costaining. HCT116 cells were grown onto a six-well plate with a density of 7×10^4 cells per well for 24 h. The cells were treated with 5 μM IrThpy@L2 for 6 and 8 h. After this, cells were carefully washed with PBS and stained with FDA (8 μg/mL) and PI (2 μg/mL) for 5 min in the dark. Then, cells were washed slowly with PBS twice, and images were captured using a fluorescence microscope.

Studies in 3D Spheroid. HCT116 cells with a density of 2×10^4 cells per well were seeded in 96 U-shaped (ultralow attachment) well plates and grown to assemble as spheroids for 72 h. Spheroids were then incubated with 5 μM IrThpy@L2 and 50 μM Cisplatin for 48 h. The integrity of the spheroids was observed for 6 days using an inverted microscope. Simultaneously, treated spheroids were stained using FDA/PI solution for 30 min in the dark at 37 °C. After that, samples were washed with PBS, and at last, images were captured using a fluorescence microscope.

https://doi.org/10.1021/acs.inorgchem.4c03950
Inorg. Chem. 2024, 63, 24709−24723

■ ASSOCIATED CONTENT

Supporting Information

The Supporting Information is available free of charge at https://pubs.acs.org/doi/10.1021/acs.inorgchem.4c03950.

NMR and HRMS spectra of L1, L2, IrPpy@L1, IrPpy@L2, IrBzq@L1, IrBzq@L2, IrThpy@L1, and IrThpy@L2. Crystallographic details of IrPpy@L2 with bond length and bond angles (PDF)

Accession Codes

Deposition Number 2310258 contains the supplementary crystallographic data for this paper. These data can be obtained free of charge via the joint Cambridge Crystallographic Data Centre (CCDC) and Fachinformationszentrum Karlsruhe Access Structures service.

■ AUTHOR INFORMATION

Corresponding Author

V. Venkatesh − *Department of Chemistry, Indian Institute of Technology Roorkee, Roorkee, Uttarakhand 247667, India;* orcid.org/0000-0001-9520-6842; Email: venkatesh.v@cy.iitr.ac.in

Authors

Tejal Dixit − *Department of Chemistry, Indian Institute of Technology Roorkee, Roorkee, Uttarakhand 247667, India*

Monika Negi − *Department of Chemistry, Indian Institute of Technology Roorkee, Roorkee, Uttarakhand 247667, India*

Complete contact information is available at: https://pubs.acs.org/10.1021/acs.inorgchem.4c03950

Author Contributions

V.V. and T.D. conceptualized the study. T.D. synthesized and characterized the complexes, and T.D. and M.N. performed all the biological studies. T.D. performed and analyzed the single crystal XRD analysis of the synthesized complex. The manuscript was written through the contributions of all authors. All authors have approved the final version of the manuscript.

Notes

The authors declare no competing financial interest.

■ ACKNOWLEDGMENTS

V.V. sincerely acknowledges Faculty Initiation Grant (FIG), IIT Roorkee, India for the funding support. T.D and M.N acknowledge University Grants Commission (UGC) and IIT Roorkee respectively for their fellowship. The authors are grateful to Dr. B.V.V.S. Pavan Kumar for providing access to the fluorescence microscope facility. The authors are also thankful to Mr. Prathapa S.J. from Bruker for assisting in solving the crystal structure, Dr. Reena Kumari and Mr. Kartikay Tyagi for their valuable suggestions while performing biological studies and Mr. Ramesh Kumar (M.Sc. Student) for assisting T.D. in ligand synthesis. We acknowledge the Institute Instrumentation Centre (IIC), IIT Roorkee for ICP-MS facility, DST-FIST for NMR and single crystal XRD facility (SR/FST/CS-II/2018/72(C)).

■ REFERENCES

(1) Beekman, A. M.; Howell, L. A. Small-molecule and peptide inhibitors of the pro-survival protein Mcl-1. *ChemMedChem.* **2016**, *11*, 802−813.

(2) Lampe, J. N. Advances in the understanding of protein-protein interactions in drug metabolizing enzymes through the use of biophysical techniques. *Front. Pharmacol.* **2017**, *8*, 521.

(3) Rao, V. S.; Srinivas, K.; Sujini, G. N.; Kumar, G. N. S. Protein-protein interaction detection: Methods and analysis. *Int. J. Proteomics.* **2014**, *2014*, 147648.

(4) Michnick, S. W. Exploring protein interactions by interaction-induced folding of proteins from complementary peptide fragments. *Curr. Opin. Struct. Biol.* **2001**, *11*, 472−477.

(5) Deng, H.; Huang, M.; Liu, H.; Zhang, H.; Liu, L.; Gao, B.; Li, X.; Li, J.; Niu, Q.; Zhang, Z.; Luan, S.; Zhang, J.; Jing, Y.; Liu, D.; Zhao, L. Development of a series of novel Mcl-1 inhibitors bearing an indole carboxylic acid moiety. *Bioorg. Chem.* **2022**, *127*, 106018.

(6) Deng, H.; Han, Y.; Liu, L.; Zhang, H.; Liu, D.; Wen, J.; Huang, M.; Zhao, L. Targeting myeloid leukemia-1 in cancer therapy: advances and directions. *J. Med. Chem.* **2024**, *67*, 5963−5998.

(7) Chen, L.; Fletcher, S. Mcl-1 inhibitors: A patent review. *Expert Opin. Ther. Pat.* **2017**, *27*, 163−178.

(8) Song, T.; Wang, Z.; Ji, F.; Feng, Y.; Fan, Y.; Chai, G.; Li, X.; Li, Z.; Zhang, Z. Deactivation of Mcl-1 by dual-function small-molecule inhibitors targeting the Bcl-2 homology 3 domain and facilitating Mcl-1 ubiquitination. *Angew. Chem., Int. Ed.* **2016**, *55*, 14250−14256.

(9) Clifton, M. C.; Dranow, D. M.; Leed, A.; Fulroth, B.; Fairman, J. W.; Abendroth, J.; Atkins, K. A.; Wallace, E.; Fan, D.; Xu, G.; Ni, Z. J.; Daniels, D.; Drie, J. V.; Wei, G.; Burgin, A. B.; Golub, T. R.; Hubbard, B. K.; Serrano-Wu, M. H. A maltose-binding protein fusion construct yields a robust crystallography platform for MCL1. *PLoS One* **2015**, *10*, No. 0125010.

(10) Negi, A.; Murphy, P. V. Development of Mcl-1 inhibitors for cancer therapy. *Eur. J. Med. Chem.* **2021**, *210*, 113038.

(11) Maeda, Y.; Takahashi, H.; Nakai, N.; Yanagita, T.; Ando, N.; Okubo, T.; Saito, K.; Shiga, K.; Hirokawa, T.; Hara, M.; Ishiguro, H.; Matsuo, Y.; Takiguchi, S. Apigenin induces apoptosis by suppressing Bcl-xl and Mcl-1 simultaneously via signal transducer and activator of transcription 3 signaling in colon cancer. *Int. J. Oncol.* **2018**, *52*, 1661−1673.

(12) Friberg, A.; Vigil, D.; Zhao, B.; Daniels, R. N.; Burke, J. P.; Garcia-Barrantes, P. M.; Camper, D.; Chauder, B. A.; Lee, T.; Olejniczak, E. T.; Fesik, S. W. Discovery of potent myeloid cell leukemia 1 (Mcl-1) inhibitors using fragment-based methods and structure-based design. *J. Med. Chem.* **2013**, *56*, 15−30.

(13) Harrison, L. R. E.; Micha, D.; Brandenburg, M.; Simpson, K. L.; Morrow, C. J.; Denneny, O.; Hodgkinson, C.; Yunus, Z.; Dempsey, C.; Roberts, D.; Blackhall, F.; Makin, G.; Dive, C. Hypoxic human cancer cells are sensitized to BH-3 mimetic−induced apoptosis via downregulation of the Bcl-2 protein Mcl-1. *J. Clin. Invest.* **2011**, *121*, 1075−1087.

(14) Zhang, Z.; Wu, G.; Xie, F.; Song, T.; Chang, X. 3-thiomorpholin-8-oxo-8h-acenaphtho[1,2-b]pyrrole-9-carbonitrile (S1) based molecules as potent, dual inhibitors of B-cell lymphoma 2 (Bcl-2) and myeloid cell leukemia sequence 1 (Mcl-1): Structure-based design and structure−activity relationship studies. *J. Med. Chem.* **2011**, *54*, 1101−1105.

(15) Zhang, S.; Zhong, X.; Yuan, H.; Guo, Y.; Song, D.; Qi, F.; Zhu, Z.; Wang, X.; Guo, Z. Interfering in apoptosis and DNA repair of cancer cells to conquer cisplatin resistance by platinum(IV) prodrugs. *Chem. Sci.* **2020**, *11*, 3829−3835.

(16) Drennen, B.; Goodis, C. C.; Bowen, N.; Yu, W.; Vickers, G.; Wilder, P. T.; MacKerell, A. D.; Fletcher, S. Scaffold hopping from indoles to indazoles yields dual MCL-1/BCL-2 inhibitors from MCL-1 selective leads. *RSC Med. Chem.* **2022**, *13*, 963−969.

(17) Yu, H.; Zhang, X.; Liu, R.; Li, H.; Xiao, X.; Zhou, Y.; Wei, C.; Yang, M.; Liao, M.; Zhao, J.; Xia, Z.; Liao, Q. Mcl-1 suppresses abasic site repair following bile acid−induced hepatic cellular DNA damage. *Tumour Biol.* **2017**, *39*, 1010428317712102.

(18) Huang, K.; Yao, H.; Yan, M.; Zhang, H.; Yuan, G.; Wang, Q.; Xue, J.; Li, J.; Chen, J. A MCL-1-targeted photosensitizer to combat triple-negative breast cancer with enhanced photodynamic efficacy,

sensitization to ROS-induced damage, and immune response. *J. Inorg. Biochem.* **2022**, *237*, 111997.
(19) Polier, G.; Ding, J.; Konkimalla, B. V.; Eick, D.; Ribeiro, N.; Köhler, R.; Giaisi, M.; Efferth, T.; Desaubry, L.; Krammer, P. H.; Li-Weber, M. Wogonin and related natural flavones are inhibitors of CDK9 that induce apoptosis in cancer cells by transcriptional suppression of Mcl-1. *Cell Death Dis.* **2011**, *2*, No. e182.
(20) Fletcher, S. MCL-1 inhibitors—where are we now (2019)? *Expert Opin. Ther. Pat.* **2019**, *29*, 909−919.
(21) Amin, S. A.; Ghosh, K.; Mondal, D.; Jha, T.; Gayen, S. Exploring indole derivatives as myeloid cell leukaemia-1 (Mcl-1) inhibitors with multi-QSAR approach: A novel hope in anti-cancer drug discovery. *New J. Chem.* **2020**, *44*, 17494−17506.
(22) Puhr, M.; Hoefer, J.; Neuwirt, H.; Eder, I. E.; Kern, J.; Schäfer, G.; Geley, S.; Heidegger, I.; Klocker, H.; Culig, Z. PIAS1 is a crucial factor for prostate cancer cell survival and a valid target in docetaxel resistant cells. *Oncotarget* **2014**, *5*, 12043−12056.
(23) Luan, S.; Ge, Q.; Chen, Y.; Dai, M.; Yang, J.; Li, K.; Liu, D.; Zhao, L. Discovery and structure-activity relationship studies of N-substituted indole derivatives as novel Mcl-1 inhibitors. *Bioorg. Med. Chem. Lett.* **2017**, *27*, 1943−1948.
(24) Lu, X.; Wu, M. F.; Wu, J. L.; Zhang, H. Q.; Liang, H.; Chen, Z. F. Platinum-based Mcl-1 inhibitor targeting mitochondria achieves enhanced antitumor activity as a single agent or in combination with ABT-199. *J. Med. Chem.* **2023**, *66*, 8705−8716.
(25) Bruncko, M.; Wang, L.; Sheppard, G. S.; Phillips, D. C.; Tahir, S. K.; Xue, J.; Erickson, S.; Fidanze, S.; Fry, E.; Hasvold, L.; Jenkins, G. J.; Jin, S.; Judge, R. A.; Kovar, P. J.; Madar, D.; Nimmer, P.; Park, C.; Petros, A. M.; Rosenberg, S. H.; Smith, M. L.; Song, X.; Sun, C.; Tao, Z. F.; Wang, X.; Xiao, Y.; Zhang, H.; Tse, C.; Leverson, J. D.; Elmore, S. W.; Souers, A. J. Structure-guided design of a series of MCL-1 inhibitors with high affinity and selectivity. *J. Med. Chem.* **2015**, *58*, 2180−2194.
(26) Liao, M.; Zhao, J.; Wang, T.; Duan, J.; Zhang, Y.; Deng, X. Role of bile salt in regulating Mcl-1 phosphorylation and chemoresistance in hepatocellular carcinoma cells. *Mol. Cancer* **2011**, *10*, 44.
(27) Wang, Z.; Xu, W.; Song, T.; Guo, Z.; Liu, L.; Fan, Y.; Wang, A.; Zhang, Z. Fragment-based design, synthesis, and biological evaluation of 1-substituted-indole-2-carboxylic acids as selective Mcl-1 inhibitors. *Arch. Pharm.* **2017**, *350*, No. 1600251.
(28) Han, J.; Goldstein, L. A.; Gastman, B. R.; Rabinovitz, A.; Rabinowich, H. Bim complex in granzyme B-mediated mitochondrial apoptosis. *J. Biol. Chem.* **2005**, *280*, 16383−16392.
(29) Venkatesh, V.; Berrocal-Martin, R.; Wedge, C. J.; Romero-Canelón, I.; Sánchez-Cano, C.; Song, J. I.; Coverdale, J. P. C.; Zhang, P.; Clarkson, G. J.; Habtemariam, A.; Magennis, S. W.; Deeth, R. J.; Sadler, P. J. Mitochondria-targeted spin-labelled luminescent iridium anticancer complexes. *Chem. Sci.* **2017**, *8*, 8271−8278.
(30) Ang, W. H.; Dyson, P. J. Classical and non-classical ruthenium-based anticancer drugs: Towards targeted chemotherapy. *Eur. J. Inorg. Chem.* **2006**, *2006*, 4003−4018.
(31) Ye, R. R.; Tan, C. P.; Ji, L. N.; Mao, Z. W. Coumarin-appended phosphorescent cyclometalated iridium(III) complexes as mitochondria-targeted theranostic anticancer agents. *Dalton Trans.* **2016**, *45*, 13042−13051.
(32) Qin, L. Q.; Zou, B. Q.; Qin, Q. P.; Wang, Z. F.; Yang, L.; Tan, M. X.; Liang, C. J.; Liang, H. Highly cytotoxic, cyclometalated iridium(III)-5-fluoro-8-quinolinol complexes as cancer cell mitochondriotropic agents. *New J. Chem.* **2020**, *44*, 7832−7837.
(33) Maurya, M. R.; Nandi, M.; Chaudhary, P. K.; Singh, S.; Avecilla, F.; Prasad, R.; Ghosh, K. Catalytic, antifungal, and antiproliferative activity studies of a new family of mononuclear $[V^{IV}O]/[V^{V}O_2]$ complexes. *Inorg. Chem.* **2024**, *63*, 714−729.
(34) Wei, F.; Liang, J.; Tan, Z.; Tang, S.; Xu, H.; Liang, H.; Shen, X. C.; Chao, H. Rhenium(I) coordinated carbon nitride as type II immunogenic cell death inducers for enhancing photoimmunotherapy against triple-negative breast cancer. *Chem. Eng. J.* **2024**, *485*, 150154.
(35) Wei, F.; Karges, J.; Gao, S.; Wang, L.; Zhang, X.; Shen, X. C.; Ji, L.; Chao, H. Two-photon phototriggering of ROS storm in ruthenium(II) coordinated carbon nitride for robust cancer immunotherapy. *Nano today* **2024**, *54*, 102066.
(36) Mani, A.; Feng, T.; Gandioso, A.; Vinck, R.; Notaro, A.; Gourdon, L.; Burckel, P.; Saubaméa, B.; Blacque, O.; Cariou, K.; Belgaied, J. E.; Chao, H.; Gasser, G. Structurally simple osmium(II) polypyridyl complexes as photosensitizers for photodynamic therapy in the near infrared. *Angew. Chem., Int. Ed.* **2023**, *135*, No. 202218347.
(37) Enslin, L. E.; Purkait, K.; Pozza, M. D.; Saubamea, B.; Mesdom, P.; Visser, H. G.; Gasser, G.; Schutte-Smith, M. Rhenium(I) tricarbonyl complexes of 1,10-phenanthroline derivatives with unexpectedly high cytotoxicity. *Inorg. Chem.* **2023**, *62*, 12237−12251.
(38) Karges, J.; Xiong, K.; Blacque, O.; Chao, H.; Gasser, G. Highly cytotoxic copper(II) terpyridine complexes as anticancer drug candidates. *Inorg. Chim. Acta* **2021**, *516*, 120137.
(39) Rubbiani, R.; Zehnder, T. N.; Mari, C.; Blacque, O.; Venkatesan, K.; Gasser, G. Anticancer profile of a series of gold(III) (2-phenyl)pyridine complexes. *ChemMedChem.* **2014**, *9*, 2781−2790.
(40) Huang, H.; Zhang, P.; Yu, B.; Chen, Y.; Wang, J.; Ji, L.; Chao, H. Targeting nucleus DNA with a cyclometalated dipyridophenazineruthenium(II) complex. *J. Med. Chem.* **2014**, *57*, 8971−8983.
(41) Cao, F.; Wang, H.; Lu, N.; Zhang, P.; Huang, H. A photoisomerizable zinc (II) complex inhibits microtubule polymerization for photoactive therapy. *Angew. Chem., Int. Ed.* **2023**, *62*, No. 202301344.
(42) Cao, J. J.; Tan, C. P.; Chen, M. H.; Wu, N.; Yao, D. Y.; Liu, X. G.; Ji, L. N.; Mao, Z. W. Targeting cancer cell metabolism with mitochondria-immobilized phosphorescent cyclometalated iridium(III) complexes. *Chem. Sci.* **2017**, *8*, 631−640.
(43) Zhang, W. Y.; Wang, Y. J.; Du, F.; He, M.; Gu, Y. Y.; Bai, L.; Yang, L. L.; Liu, Y. J. Evaluation of anticancer effect in vitro and in vivo of iridium(III) complexes on gastric carcinoma SGC-7901 cells. *Eur. J. Med. Chem.* **2019**, *178*, 401−416.
(44) Hockey, S. C.; Barbante, G. J.; Francis, P. S.; Altimari, J. M.; Yoganantharajah, P.; Gibert, Y.; Henderson, L. C. A comparison of novel organo-iridium(III) complexes and their ligands as a potential treatment for prostate cancer. *Eur. J. Med. Chem.* **2016**, *109*, 305−313.
(45) Xie, L.; Shi, L.; Xiong, K.; Guan, R.; Chen, Y.; Long, J.; Ji, L.; Chao, H. Synthesis, subcellular localization and anticancer mechanism studies of unsymmetrical iridium(III) complexes. *Eur. J. Inorg. Chem.* **2023**, *26*, No. 202300001.
(46) Li, X.; Wang, Z.; Hao, X.; Zhang, J.; Zhao, X.; Yao, Y.; Wei, W.; Cai, R.; He, C.; Duan, C.; Guo, Z.; Zhao, J.; Wang, X. Optically pure double-stranded dinuclear Ir(III) metallohelices enabled chirality-induced photodynamic responses. *J. Am. Chem. Soc.* **2023**, *145*, 14766−14775.
(47) Sun, Y.; Liu, J.; Li, Q.; Zhang, X.; Cao, Z.; Bu, L.; Cao, S.; Liu, X.; Yuan, X. A.; Liu, Z. Studies of anticancer activities in vitro and in vivo for butyltin(IV)−iridium(III) imidazole−phenanthroline complexes with aggregation-induced emission properties. *Inorg. Chem.* **2024**, *63*, 14641−14655.
(48) Wang, F. X.; Chen, M. H.; Hu, X. Y.; Ye, R. R.; Tan, C. P.; Ji, L. N.; Mao, Z. W. Ester-modified cyclometalated iridium(III) complexes as mitochondria-targeting anticancer agents. *Sci. Rep.* **2016**, *6*, 38954.
(49) Yuan, Y.; Zhang, Y.; Chen, J.; Huang, C.; Liu, H.; Li, W.; Liang, L.; Wang, Y.; Liu, Y. Synthesis, biological evaluation of novel iridium(III) complexes targeting mitochondria toward melanoma B16 cells. *Eur. J. Med. Chem.* **2023**, *247*, 115046.
(50) Cao, J. J.; Zheng, Y.; Wu, X. W.; Tan, C. P.; Chen, M. H.; Wu, N.; Ji, L. N.; Mao, Z. W. Anticancer cyclometalated iridium(III) complexes with planar ligands: Mitochondrial DNA damage and metabolism disturbance. *J. Med. Chem.* **2019**, *62*, 3311−3322.
(51) Qiao, L.; Liu, J.; Kuang, S.; Liao, X.; Kou, J.; Ji, L.; Chao, H. A mitochondrion-targeted BODIPY-Ir(III) conjugate as a photoinduced ROS generator for the oxidative destruction of triple-negative breast cancer cells. *Dalton Trans.* **2021**, *50*, 14332−14341.
(52) Sun, Q.; Wang, Y.; Fu, Q.; Ouyang, A.; Liu, S.; Wang, Z.; Su, Z.; Song, J.; Zhang, Q.; Zhang, P.; Lu, D. Sulfur-coordinated organoiridium(III) complexes exert breast anticancer activity via

https://doi.org/10.1021/acs.inorgchem.4c03950
Inorg. Chem. 2024, 63, 24709−24723

inhibition of Wnt/β-Catenin signaling. *Angew. Chem. In. Ed.* **2021**, *133*, 4891−4898.
(53) Ouyang, M.; Zeng, L.; Huang, H.; Jin, C.; Liu, J.; Chen, Y.; Ji, L.; Chao, H. Fluorinated cyclometalated iridium(III) complexes as mitochondria-targeted theranostic anticancer agents. *Dalton Trans.* **2017**, *46*, 6734−6744.
(54) Wu, N.; Cao, J. J.; Wu, X. W.; Tan, C. P.; Ji, L. N.; Mao, Z. W. Iridium(III) complexes with five-membered heterocyclic ligands for combined photodynamic therapy and photoactivated chemotherapy. *Dalton Trans.* **2017**, *46*, 13482−13491.
(55) Liu, B.; Huang, X.; Hu, M.; Chen, Z.; Zhang, W.; Li, Y. Mitochondria-targeted cyclometalated iridium (III) complex for H_2S-responsive intracellular redox regulation as potent photo-oxidation anticancer agent. *J. Biol. Inorg. Chem.* **2022**, *27*, 641−651.
(56) Chen, B. B.; Pan, N. L.; Liao, J. X.; Huang, M. Y.; Jiang, D. C.; Wang, J. J.; Qiu, H. J.; Chen, J. X.; Li, L.; Sun, J. Cyclometalated iridium(III) complexes as mitochondria-targeted anticancer and antibacterial agents to induce both autophagy and apoptosis. *J. Inorg. Biochem.* **2021**, *219*, 111450.
(57) Li, Y.; Liu, B.; Xu, C. X.; He, L.; Wan, Y. C.; Ji, L. N.; Mao, Z. W. Mitochondria-targeted phosphorescent cyclometalated iridium-(III) complexes: synthesis, characterization, and anticancer properties. *J. Biol. Inorg. Chem.* **2020**, *25*, 597−607.
(58) He, L.; Wang, K. N.; Zheng, Y.; Cao, J. J.; Zhang, M. F.; Tan, C. P.; Ji, L. N.; Mao, Z. W. Cyclometalated iridium(III) complexes induce mitochondria-derived paraptotic cell death and inhibit tumor growth *in vivo*. *Dalton Trans.* **2018**, *47*, 6942−6953.
(59) Zhang, W. Y.; Banerjee, S.; Hughes, G. M.; Bridgewater, H. E.; Song, J. I.; Breeze, B. G.; Clarkson, G. J.; Coverdale, J. P. C.; Sanchez-Cano, C.; Ponte, F.; Sicilia, E.; Sadler, P. J. Ligand-centred redox activation of inert organoiridium anticancer catalysts. *Chem. Sci.* **2020**, *11*, 5466−5480.
(60) Katlenok, E. A.; Rozhkov, A. V.; Ramazanov, R. R.; Valiev, R. R.; Levin, O. V.; Goryachiy, D. O.; Taydakov, I. V.; Kuznetsov, M. L.; Kukushkin, V. Y. Photo- and electroluminescent neutral iridium(III) complexes bearing imidoylamidinate ligands. *Inorg. Chem.* **2022**, *61*, 8670−8684.
(61) Qiu, K.; Ouyang, M.; Liu, Y.; Huang, H.; Liu, C.; Chen, Y.; Ji, L.; Chao, H. Two-photon photodynamic ablation of tumor cells by mitochondria-targeted iridium(III) complexes in aggregate states. *J. Mater. Chem. B* **2017**, *5*, 5488−5498.
(62) Hao, J.; Zhang, H.; Tian, L.; Yang, L.; Zhou, Y.; Zhang, Y.; Liu, Y.; Xing, D. Evaluation of anticancer effects in vitro of new iridium(III) complexes targeting the mitochondria. *J. Inorg. Biochem.* **2021**, *221*, 111465.
(63) Yang, J.; Wang, W. T.; Shi, Z. D.; Yang, R.; Liao, X. L.; Yang, B.; Gao, C. Z. Near-infrared phosphorescent cyclometalated platinum (II) and iridium (III) complexes with metformin moiety: Design and study towards anticancer theranostic agents. *J. Inorg. Biochem.* **2022**, *237*, 111992.
(64) Bi, X. D.; Yang, R.; Zhou, Y. C.; Chen, D.; Li, G. K.; Guo, Y. X.; Wang, M. F.; Liu, D.; Gao, F. Cyclometalated iridium(III) complexes as high-sensitivity two-photon excited mitochondria dyes and near-infrared photodynamic therapy agents. *Inorg. Chem.* **2020**, *59*, 14920−14931.
(65) Xiang, H.; Chen, H.; Tham, H. P.; Phua, S. Z. F.; Liu, J. G.; Zhao, Y. Cyclometalated iridium(III)-complex-based micelles for glutathione-responsive targeted chemotherapy and photodynamic therapy. *ACS Appl. Mater. Interfaces* **2017**, *9*, 27553−27562.
(66) Xiong, X.; Huang, K. B.; Wang, Y.; Cao, B.; Luo, Y.; Chen, H.; Yang, Y.; Long, Y.; Liu, M.; Chan, A. S. C.; Liang, H.; Zou, T. Target profiling of an iridium(III)-based immunogenic cell death inducer unveils the engagement of unfolded protein response regulator BiP. *J. Am. Chem. Soc.* **2022**, *144*, 10407−10416.
(67) Kench, T.; Rahardjo, A.; Terrones, G. G.; Bellamkonda, A.; Maher, T. E.; Storch, M.; Kulik, H. J.; Vilar, R. A semi-automated, high-throughput approach for the synthesis and identification of highly photo-cytotoxic iridium complexes. *Angew. Chem., Int. Ed.* **2024**, *63*, No. 202401808.
(68) Cañada, L. M.; Kölling, J.; Wen, Z.; Wu, J. I. C.; Teets, T. S. Cyano-isocyanide iridium(III) complexes with pure blue phosphorescence. *Inorg. Chem.* **2021**, *60*, 6391−6402.
(69) Na, H.; Teets, T. S. Highly luminescent cyclometalated iridium complexes generated by nucleophilic addition to coordinated isocyanides. *J. Am. Chem. Soc.* **2018**, *140*, 6353−6360.
(70) Bevernaegie, R.; Wehlin, S. A. M.; Elias, B.; Troian-Gautier, L. A roadmap towards visible light mediated electron transfer chemistry with iridium(III) complexes. *ChemPhotoChem.* **2021**, *5*, 217−234.
(71) Lai, P. N.; Yoon, S.; Teets, T. S. Efficient near-infrared luminescence from bis-cyclometalated iridium(III) complexes with rigid quinoline-derived ancillary ligands. *Chem. Commun.* **2020**, *56*, 8754−8757.
(72) Zhao, Z.; Gao, P.; Ma, L.; Chen, T. A highly X-Ray sensitive iridium prodrug for visualized tumor radiochemotherapy. *Chem. Sci.* **2020**, *11*, 3780−3789.
(73) Maity, A.; Le, L. Q.; Zhu, Z.; Bao, J.; Teets, T. S. Steric and electronic influence of aryl isocyanides on the properties of iridium(III) cyclometalates. *Inorg. Chem.* **2016**, *55*, 2299−2308.
(74) Li, Y.; Tan, C. P.; Zhang, W.; He, L.; Ji, L. N.; Mao, Z. W. Phosphorescent iridium(III)-bis-N-heterocyclic carbene complexes as mitochondria-targeted theranostic and photodynamic anticancer agents. *Biomater.* **2015**, *39*, 95−104.
(75) Ye, R. R.; Tan, C. P.; He, L.; Chen, M. H.; Ji, L. N.; Mao, Z. W. Cyclometalated Ir(III) complexes as targeted theranostic anticancer therapeutics: combining HDAC inhibition with photodynamic therapy. *Chem. Commun.* **2014**, *50*, 10945−10948.
(76) Ye, R. R.; Cao, J. J.; Tan, C. P.; Ji, L. N.; Mao, Z. W. Valproic acid-functionalized cyclometalated iridium(III) complexes as mitochondria-targeting anticancer agents. *Chem.—Eur. J.* **2017**, *23*, 15166−15176.
(77) Madak, J. T.; Neamati, N. Membrane permeable lipophilic cations as mitochondrial directing groups. *Curr. Top. Med. Chem.* **2015**, *15*, 745−766.
(78) Kuang, S.; Liao, X.; Zhang, X.; Rees, T. W.; Guan, R.; Xiong, K.; Chen, Y.; Ji, L.; Chao, H. FerriIridium: A lysosome-targeting iron(III)-activated iridium(III) prodrug for chemotherapy in gastric cancer cells. *Angew. Chem., Int. Ed.* **2020**, *59*, 3315−3321.
(79) He, L.; Li, Y.; Tan, C. P.; Ye, R. R.; Chen, M. H.; Cao, J. J.; Ji, L. N.; Mao, Z. W. Cyclometalated iridium(III) complexes as lysosome-targeted photodynamic anticancer and real-time tracking agents. *Chem. Sci.* **2015**, *6*, 5409−5418.
(80) Kabir, E.; Wu, Y.; Sittel, S.; Nguyen, B. L.; Teets, T. S. Improved deep-red phosphorescence in cyclometalated iridium complexes *via* ancillary ligand modification. *Inorg. Chem. Front.* **2020**, *7*, 1362−1373.
(81) Liu, M.; Luo, Y.; Yan, J.; Xiong, X.; Xing, X.; Kim, J. S.; Zou, T. Photoactivation of boronic acid prodrugs via a phenyl radical mechanism: iridium(III) anticancer complex as an example. *J. Am. Chem. Soc.* **2023**, *145*, 10082−10091.
(82) Millard, M.; Gallagher, J. D.; Olenyuk, B. Z.; Neamati, N. A Selective mitochondrial-targeted chlorambucil with remarkable cytotoxicity in breast and pancreatic cancers. *J. Med. Chem.* **2013**, *56*, 9170−9179.
(83) Prag, H. A.; Kula-Alwar, D.; Pala, L.; Caldwell, S. T.; Beach, T. E.; James, A. M.; Saeb-Parsy, K.; Krieg, T.; Hartley, R. C.; Murphy, M. P. Selective delivery of dicarboxylates to mitochondria by conjugation to a lipophilic cation via a cleavable linker. *Mol. Pharmaceutics* **2020**, *17*, 3526−3540.
(84) Kuang, S.; Wei, F.; Karges, J.; Ke, L.; Xiong, K.; Liao, X.; Gasser, G.; Ji, L.; Chao, H. Photodecaging of a mitochondria-localized iridium(III) endoperoxide complex for two-photon photoactivated therapy under hypoxia. *J. Am. Chem. Soc.* **2022**, *144*, 4091−4101.
(85) Zhou, A. M.; Wang, M. M.; Su, Y.; Yu, Z. H.; Liu, H. K.; Su, Z. Switching the mode of cell death between apoptosis and autophagy by histone deacetylase 6 inhibition levels. *ChemMedChem.* **2023**, *18*, No. e202200614.
(86) Peng, W.; Hegazy, A. M.; Jiang, N.; Chen, X.; Qi, H. X.; Zhao, X. D.; Pu, J.; Ye, R. R.; Li, R. T. Identification of two mitochondrial

targeting cyclometalated iridium(III) complexes as potent anti-glioma stem cells agents. *J. Inorg. Biochem.* **2020**, *203*, 110909.
(87) Negi, M.; Dixit, T.; Venkatesh, V. Ligand dictated photosensitization of iridium(III) dithiocarbamate complexes for photodynamic therapy. *Inorg. Chem.* **2023**, *62*, 20080−20095.
(88) Huang, T.; Yu, Q.; Liu, S.; Zhang, K. Y.; Huang, W.; Zhao, Q. Rational design of phosphorescent iridium(III) complexes for selective glutathione sensing and amplified photodynamic therapy. *ChemBioChem.* **2019**, *20*, 576−586.
(89) Lai, P. N.; Brysacz, C. H.; Alam, M. K.; Ayoub, N. A.; Gray, T. G.; Bao, J.; Teets, T. S. Highly efficient red-emitting bis-cyclometalated iridium complexes. *J. Am. Chem. Soc.* **2018**, *140*, 10198−10207.
(90) Zhu, Z.; Wei, L.; Lai, Y.; Carter, O. W. L.; Banerjee, S.; Sadler, P. J.; Huang, H. Photocatalytic glucose-appended bio-compatible Ir(III) anticancer complexes. *Dalton Trans.* **2022**, *51*, 10875−10879.
(91) Zhang, P.; Chiu, C. K. C.; Huang, H.; Lam, Y. P. Y.; Habtemariam, A.; Malcomson, T.; Paterson, M. J.; Clarkson, G. J.; O'Connor, P. B.; Chao, H.; Sadler, P. J. Organoiridium photosensitizers induce specific oxidative attack on proteins within cancer cells. *Angew. Chem., Int. Ed.* **2017**, *56*, 14898−14902.
(92) Zhou, W.; Hu, J.; Tang, H.; Wang, D.; Huang, X.; He, C.; Zhu, H. Small interfering RNA targeting mcl-1 enhances proteasome inhibitor-induced apoptosis in various solid malignant tumors. *BMC Cancer* **2011**, *11*, 485.
(93) Bolesta, E.; Pfannenstiel, L. W.; Demelash, A.; Lesniewski, M. L.; Tobin, M.; Schlanger, S. E.; Nallar, S. C.; Papadimitriou, J. C.; Kalvakolanu, D. V.; Gastman, B. R. Inhibition of Mcl-1 promotes senescence in cancer cells: Implications for preventing tumor growth and chemotherapy resistance. *Mol. Cell. Biol.* **2012**, *32*, 1879−1892.
(94) Zheng, G. W.; Tang, M. M.; Shu, C. Y.; Xin, W. X.; Zhang, Y. H.; Chi, B. B.; Shi, M. R.; Guo, X.; Zhang, Z. Z.; Lian, X. Y. A small natural molecule CADPE kills residual colorectal cancer cells by inhibiting key transcription factors and translation initiation factors. *Cell Death Dis.* **2020**, *11*, 982.
(95) Park, S. H.; Lee, D. H.; Kim, J. L.; Lee, S. I.; Kim, B. R.; Na, Y. J.; Lee, S. Y.; Kim, H. J.; Joung, S. Y.; Kang, S.; Oh, S. C. Abstract 3497: Metformin enhances TRAIL-induced apoptosis by Mcl-1 degradation via mule in colorectal cancer cells. *Cancer Res.* **2016**, *76*, 3497.
(96) Basseville, A.; Preisser, L.; Trecesson, S. C.; Boisdron-Celle, M.; Gamelin, E.; Coqueret, O.; Morel, A. Irinotecan induces steroid and xenobiotic receptor (SXR) signaling to detoxification pathway in colon cancer cells. *Mol. Cancer* **2011**, *10*, 80.
(97) Figueiredo, P. R.; González, R. D.; Carvalho, A. T. P. Insights into the degradation of polymer−drug conjugates by an overexpressed enzyme in cancer cells. *J. Med. Chem.* **2023**, *66*, 2761−2772.
(98) Ozsan, C.; Kailass, K.; Digby, E. M.; Almammadov, T.; Beharry, A. A.; Kolemen, S. Selective detection of carboxylesterase 2 activity in cancer cells using an activity-based chemiluminescent probe. *Chem. Commun.* **2022**, *58*, 10929−10932.
(99) Liu, X.; Li, X.; Dong, P.; Wu, Z.; Gao, J.; Wang, Q. Near-infrared emission tracks inter-individual variability of carboxylesterase-2 via a novel molecular substrate. *Mikrochim. Acta* **2020**, *187*, 313.
(100) Su, L.; Gao, K.; Tian, Y.; Xiao, X.; Lu, C.; Xu, J.; Yan, X. Mitochondrial esterase activity measured at the single organelle level by nano-flow cytometry. *Anal. Chem.* **2024**, *96*, 810−820.
(101) Wang, B.; Ni, Z.; Dai, X.; Qin, L.; Li, X.; Xu, L.; Lian, J.; He, F. The Bcl-2/xL inhibitor ABT-263 increases the stability of Mcl-1 mRNA and protein in hepatocellular carcinoma cells. *Mol. Cancer* **2014**, *13*, 98.
(102) Han, J.; Goldstein, L. A.; Gastman, B. R.; Rabinovitz, A.; Rabinowich, H. Disruption of Mcl-1.Bim complex in granzyme B-mediated mitochondrial apoptosis. *J. Biol. Chem.* **2005**, *280*, 16383−16392.
(103) Carrasco, A. C.; Rodríguez-Fanjul, V.; Habtemariam, A.; Pizarro, A. M. Structurally strained half-sandwich iridium(III) complexes as highly potent anticancer agents. *J. Med. Chem.* **2020**, *63*, 4005−4021.
(104) Wang, W.; Wang, P.; Liao, X.; Yang, B.; Gao, C.; Yang, J. A series of planar phosphorescent cyclometalated platinum(II) complexes as new anticancer theranostic agents that induce oncosis. *J. Med. Chem.* **2023**, *66*, 13103−13115.
(105) Rayes, S. M. E.; Aboelmagd, A.; Gomaa, M. S.; Fathalla, W.; Ali, I. A. I.; Pottoo, F. H.; Khan, F. A. Newly synthesized 3-(4-chlorophenyl)-3-hydroxy-2,2-dimethyl-propionic acid methyl ester derivatives selectively inhibit the proliferation of colon cancer cells. *RSC Adv.* **2020**, *10*, 8825−8841.
(106) Tartagni, O.; Borók, A.; Mensà, E.; Bonyár, A.; Monti, B.; Hofkens, J.; Porcelli, A. M.; Zuccheri, G. Microstructured soft devices for the growth and analysis of populations of homogenous multicellular tumor spheroids. *Cell. Mol. Life Sci.* **2023**, *80*, 93.
(107) Novohradsky, V.; Marco, A.; Markova, L.; Cutillas, N.; Ruiz, J.; Brabec, V. Ir(III) compounds containing a Terdentate Ligand Are Potent Inhibitors of Proliferation and Effective Antimetastatic Agents in Aggressive Triple-Negative Breast Cancer Cells. *J. Med. Chem.* **2023**, *66*, 9766−9783.

https://doi.org/10.1021/acs.inorgchem.4c03950
Inorg. Chem. 2024, 63, 24709−24723